# Supporting Information

**Bicontinuous-phase electrolyte for highly reversible Zn metal anode working at ultralow temperature**

Mi Xu,[a] Beinuo Zhang,[a] Yudong Sang,[a] Dan Luo,[a] Rui Gao,[b] Qianyi Ma,[b] Haozhen Dou*[ab] and Zhongwei Chen*[ab]

M. Xu, B. Zhang, Y. Sang, D. Luo, H. Dou, Z. Chen
State Key Laboratory of Catalysis, Power Battery & System Research Center, Dalian Institute of Chemical Physics, Chinese Academy of Sciences, Dalian, 110623, China.
E-mail: haozhen@dicp.ac.cn
E-mail: zwchen@dicp.ac.cn

R. Gao, Q. Ma, H. Dou, Z. Chen
Department of Chemical Engineering, University of Waterloo, Waterloo, ON N2L 3G1, Canada
E-mail: zhwchen@uwaterloo.ca

**Experimental details**

**1.1. Materials**

Zinc trifluoromethylsulfonate (Zn(OTf)$_2$, ≥98%), dimethyl sulfoxide (DMSO, GC, >99.8%), N-methyl-2-pyrrolidone (HPLC, ≥99%), vanadium(V) oxide (≥99.95%), hydrogen peroxide (30 wt. % in H$_2$O), ammonium persulfate (≥ 98.0%), aniline (≥ 99.5%) and hydrochloric acid (HCl, 36.5-38.0%) were all purchased from Sigma-Aldrich and used as received.

2 m Zn(OTf)$_2$ electrolyte was prepared by dissolving 6 mmol Zn(OTf)$_2$ into 3 mL deionized water, where m represents the ratio of mol (zinc salt) to total volume of solvent without considering volume change. A family of hybrid electrolytes were fabricated by adding 6 mmol Zn(OTf)$_2$ into 3 mL DMSO-H$_2$O mixed solvent with different volume ratios of 2:1, 1:1 and 1:2, which are denoted as HD21, HD11 and HD12 respectively.

Regarding to V$_2$O$_5$ cathodes, the commercial V$_2$O$_5$ powder was purified by a typical hydrothermal method. 2 mmol V$_2$O$_5$ was dispersed in 80 mL deionized water with stirring for 10 minutes. Subsequently, 2 mL H$_2$O$_2$ was slowly added dropwise to the solution under vigorous stirring, and continue stirring until the V$_2$O$_5$ powder was completely dissolved. Afterward, the obtained solution was transferred into 100 ml Teflon-lined autoclave, followed by hydrothermal reaction at 120 ℃ for 6 hours. Finally, the V$_2$O$_5$ particles was collected after a 96-hour freeze-dried in vacuum. The V$_2$O$_5$ cathode was fabricated by doctor blading the slurry of V$_2$O$_5$ powder, Super P carbon as conductive agent and polyvinylidene fluoride as binder in a weight ratio of 7:2:1 with N-methyl-2-pyrrolidone as solvent on ultrathin carbon cloth (> 99.99%, 20 μm). The slurry-coated carbon cloth was vacuum-dried at 70 °C overnight, and was then punched or cut into variform V$_2$O$_5$ cathodes for battery assembly, for example, the 12 mm circular V$_2$O$_5$ cathodes for the coin-type batteries and rectangle V$_2$O$_5$ cathodes (5 cm ×10 cm) for pouch batteries. The mass loading of V$_2$O$_5$ was 2 mg cm$^{-2}$ for coin batteries and 14 mg/cm$^2$ for high loading test.

As for Zn anode, the commercial Zn metal foil with different thickness was used and directly used Zn anodes. For depth of discharge measurement, 20 μm ultrathin Zn foil was used as Zn anode, while for other batteries, 100 μm Zn foil were used.

**1.2. Electrochemical measurements**

All batteries were assembled in an open environment, and their electrochemical performances were tested in C2032-type coin cells with LAND-CT2001A battery testing system. The Zn-Zn symmetric cells, Zn-Cu cells, and Zn-Ti cells were assembled by sandwiching glass fiber separator (Whatman, GF/D) between two metal electrodes (100 μm Zn

metal electrode, 20 μm Cu metal electrode or Ti electrode), and the amount of electrolyte for each cell was controlled to be 100 μL. The $Zn$-$V_2O_5$ full batteries were assembled with zinc metal anode, $V_2O_5$ cathode, 30 μL electrolyte, and glass filter (Whatman, GF/A). The Zn-Zn symmetric cells were used to evaluate the cycling stability of Zn plating/stripping in different electrolytes at the current densities of 0.5, 1, 2, 5, 10 and 20 mA·cm⁻² in the voltage range of -1.0 V -1.0 V. Zn‖Cu cells and Zn-Ti cells were assembled to evaluate the Coulombic efficiency (CE) with a cut-off potential of 1.0 V. The cycling performance and rate capability of $Zn$/$V_2O_5$ full batteries were tested between the voltages of 0.3 V~1.8 V at the current densities of 0.5 A·g-1, 1 A·g-1, 3 A·g-1, 5 A·g-1, 8 A·g-1, 10 A·g-1 and 15 A·g-1 (calculated based on the mass of active material in the cathode). The low-temperature battery performances were measured in KST-150C high and low temperature test chamber with the working temperature range of -60 ℃~25 ℃.

The linear scanning voltammetry (LSV), electrochemical impedance spectroscopy (EIS), chronoamperograms (CAs) and cyclic voltammetry (CV) curves were conducted on a VMP3 Bio-Logic electrochemical workstation. LSV was collected based on a three-electrode cell with Zn as reference electrode, Ti as both working and counter electrodes over the voltage range of -0.5 V~3.0 V at a scan rate of 1 mV·s⁻¹. EIS test using Ti-Ti symmetric cells was conducted over the frequency range of 10 mHz ~100 kHz, and the ionic conductivity was calculated with the following equation: $\sigma = \dfrac{l}{RS}$, where l is the electrolyte thickness, R denotes the bulk resistance, S denotes the area of the electrode. CA curve of Zn electrode in electrolyte was tested using Zn-Zn battery at a fixed overpotential of -150 mV. The scan for CV testing of Zn-Ti battery was carried out in the range of -0.2 V-0.3 V with the scan rate of 1 mV·s⁻¹. The transference number of $Zn^{2+}$ ($tZn^{2+}$) was performed by chronoamperometry and calculated by the following equation: $t_{Zn2+} = \dfrac{I_S(\Delta V - I_0 R_0)}{I_0(\Delta V - I_S R_S)}$, where $I_0$ and $R_0$ represent the current and resistance before polarization, $I_S$ and $R_S$ represent the current and resistance after polarization, $\Delta V$ corresponds to the applied polarization potential (20 mV). The Arrhenius activation energy (Ea) was calculated according to the following equation: $\dfrac{1}{R_{ct}} = A exp(\dfrac{-E_a}{RT})$, where Rct is the interface resistance, A and R are the frequency factor and gas constant, T signifies the absolute temperature.

## 1.3. Materials characterization

1H nuclear magnetic resonance (NMR) and 19F NMR spectra were collected from the JEOL JNM ECZ600R spectrometer (Japan) with a self-evaporating cryogenic system. For NMR experiment, the electrolyte was injected into the outer layer of the coaxial NMR tube with the deuterated reagent used as the field frequency lock inside the inner layer of the tube. Deuterated dimethyl sulfoxide (d6-DMSO) was used for room-temperature test and chloroform ($CDCl_3$) with much more lower freezing point was used for variable-temperature test. Fourier transform infrared (FTIR) spectra were performed using Nicolet iS50 FTIR spectrometer equipped with a diamond ATR accessory. Raman spectra was obtained on a Renishaw inVia confocal Raman microscope with a laser emitting at 532 nm. Differential scanning calorimetry (DSC) was tested using a TA Q2000 facility) equipped with cryogenic determination to detected the freezing point of the electrolytes., which was determined by taking the onset melting temperature of the endothermic change from the thermal baseline. Two-dimensional small-angle/wide-angle X-ray scattering (2D-SWAXS) spectra are obtained in Suzhou Vacuum Interconnected Nanotech Workstation. Synchrotron radiation X-ray absorption near-edge structure (XANES) spectra and Fourier transformation of extended X-ray absorption fine structure (EXAFS) spectra were acquired on BL11B beamline at Shanghai Synchrotron Radiation Facility. Contact angle test was performed on a Dataphysics OCA15 apparatus. And the ignition test was conducted by burning the electrolyte-socked glass fiber for 10 seconds. In-situ optical microscope characterization of Zn plating behavior on the surface of Zn electrode under different electrolytes was performed on the AxioVert. A1 (ZEISS) equipment combining with a digital camera. The transparent Zn||Zn symmetric cell was tested for Zn stripping/plating using the LAND electrochemical workstation and the stripping/plating current density was 5.0 mA cm$^{-2}$. Scanning electron microscopy (SEM) with corresponding energy dispersive spectrometer (EDS) mappings were examined by Hitachi S-4800 Field-emission scanning electron microscopy. X-ray diffraction (XRD) patterns were acquired with X'Pert Pro X-ray diffractometer with monochromatized Cu Kα radiation (λ = 1.5406 Å) at a scan rate of 10° min$^{-1}$. Two-dimensional synchrotron X-ray diffraction (2D-XRD) images were performed on VESPERS beamline at the Canadian Light Sources. STXM measurements were performed at the SM beamline in Canadian Light Source. X-ray Computed Tomography conducted at the tomography station at BMIT-BM beamline in Canadian Light Sources. X-ray photoelectron spectroscopy (XPS) was conducted on Thermo-Fisher Scientific ESCALAB Xi X-ray photoelectron spectrometer under the voltage of 1 KV, and for depth profiling, the Argon cluster ion gun with 1 KeV ion energy was used to sputter 1×1 mm$^2$ areas centered around the analyzed areas (200×200 μm$^2$). Time-of-flight secondary ion mass spectrometry (TOF-SIMS) was

4

carried out using TOF.SIMS5-100 and the signal was collected with the sputtering of $Cs^+$ ion beam (1 KeV ion energy, ~40 nA measured sample current) during the period of 1600 seconds in the area of $50 \times 50$ μm$^2$. Focused ion beam microscope (FIB) was measured by FEI Scios with liquid Ga ion source in depth of 10 um at beam intensity of 3 nA. Before sputtering, Pt and C were uniformly deposited on the surface of the analyzed areas.

**1.4. Molecular dynamics simulation**

Density functional theory (DFT) calculations and molecular dynamic (MD) simulations were applied to investigate the solvation structures, interaction energy between solution components and de-solvation energy of dominant solvation sheaths for different electrolyte systems.

*1.4.1. Binding energy between electrolyte components*

The binding energies between solution components were respectively calculated by DMol3 module in materials studio (MS) 8.0. Firstly, the generalized gradient approximation (GGA) with Perdew–Burke–Ernzerhof (PBE) exchange-correlation functional was employed to fully relax each component. The double-numeric quality basis sets with polarization functions were used. The global orbital cutoff was 4.4 Å. The iterative tolerances for energy change, force and displacements were $1 \times 10^{-5}$ Ha, 0.002 Ha Å$^{-1}$ and 0.005 Å, respectively. In the self-consistent field (SCF) procedure, $10^{-6}$ a.u. was used for the convergence standard electron density. After structure optimization, the Adsorption Locator Tools[1] in MS were used to construct interaction pairs. Then each pair was freely optimized by DMol3 module. Finally, single point energy calculation was executed, and meanwhile electron density and electrostatic potential (ESP) were outputted. The isosurfaces with the ESP mapped onto the electron density were displayed, in which the isosurface level was set to be 0.017 a.u[2]. The binding energies $E_b$ were calculated according to the following equation:

$$E_b = E_{AB} - E_A - E_B$$

Where $E_{AB}$, $E_A$ and $E_B$ are the energies of the interaction pair, isolated component A and B.

*1.4.2. Molecular dynamic (MD) simulations for solvation structure analysis*

The electrolyte systems consisting of different numbers of compositions were respectively constructed into cubic simulation boxes. All MD simulations were carried out using the LAMMPS package[3]. The universal force field (UFF)[4] was adopted to describe the bond and non-bond interaction. Water molecule was described by the SPC model[5]. Van der Waals and Coulomb interactions were calculated using a cut-off value of 12.5 Å. Equations of motion were

integrated by leapfrog algorithm with a time step of 1 fs. After energy minimization, each system was fully optimized under periodic boundary conditions for 400 ps in the NPT (P = 1 atmosphere, T = 298 K) ensemble using the Nose-Hoover thermostat and barostat, which was long enough for system temperature, potential and total energy to get stable. After reaching equilibrium state, another 400 ps simulation under NVT (T = 298 K) ensemble was performed to extract data. The dynamic trajectory for each model was outputted at 4 ps interval and used for radial distribution function (RDF) and solvation structure analysis. The model display in ball and stick style and corresponding surface mesh analysis were carried out using by OVITO. The model display in space filling style was visualized by VMD[6]. The coordination number $N_i$ of molecules $i$ in the first solvation shell surrounding $Zn^{2+}$ was calculated as:

$$N_i = 4\pi\rho \int_0^{R_M} g(r)r^2 dr$$

in which $R_M$ is the distance of the first minimum following the first peak in the RDF $g(r)$ and $\rho$ is the number density of molecules $i$[7]. Furthermore, configurations of solvation structure and corresponding proportion were analyzed using by MD Analysis software package[8].

*1.4.3. Desolvation energy calculation*

After obtaining dominant solvation structures from MD Analysis, each configuration was fully optimized by DMol3 module in MS. The desolvation energies $\Delta E_{de}$ were calculated according to the following equation:

$$\Delta E_{de} = E_{total} - E_{solvent} - E_{Zn^{2+}}$$

Where $E_{total}$ is the total energy of the solvation structure, $E_{solvent}$ and $E_{Zn^{2+}}$ are the energies of isolated solvent surrounding $Zn^{2+}$ and $Zn^{2+}$, respectively.

**Tables**

**Table S1. Low-temperature performance of Zn//Zn symmetrical cell based on hybrid electrolytes.**

| Reference | Temperature (ºC) | Current density (mA/cm²) | Areal capacity (mAh/cm²) | Life span (h) |
|---|---|---|---|---|
| Angew. Chem. 2021, 133, 7442 – 7451 | -10 | 1 | 0.5 | 200 |
| Energy Environ. Sci., 2020, 13, 3527-3535 | -20 | 2 | 1 | 80 |
| Adv. Mater. 2022, 34, 2207344 | -40 | 0.5 | 0.5 | 4000 |
| Nat Sustain 5, 205–213 (2022) | -30 | 1 | 0.5 | 100 |
| Adv. Energy Mater. 2023, 2301466 | -40 | 1 | 0.5 | 100 |
|  | -50 | 0.5 | 0.25 | 100 |
| ACS Energy Lett. 2023, 8, 1613−1625 | -20 | 0.5 | 0.5 | 2000 |
| Energy Storage Materials 52 (2022) 52–60 | 0 | 2 | 2 | 1200 |
|  | -18 | 1 | 1 | 400 |
| Small 2021, 2103195 | -20 | 0.5 | 1 | 1200 |
|  | -20 | 2 | 1 | 120 |
| Energy Storage Materials 42 (2021) 517–525 | 0 | 1 | 1 | 2000 |
|  | -25 | 1 | 1 | 2000 |
| Chemical Engineering Journal 433 (2022) 134589 | -40 | 1 | 1 | 500 |
|  | -40 | 3 | 1 | 500 |
|  | -40 | 5 | 1 | 500 |
|  | -20 | 10 | 1 | 500 |
| Adv. Mater. 2024, 2402245 | -10 | 1 | 1 | 4000 |
| Angew. Chem. Int. Ed. 2023, 62, e202315834 | -40 | 0.25 | 0.25 | 2000 |
| **This work** | **-20** | **0.5** | **0.5** | **4700** |
| **This work** | **-40** | **0.5** | **0.5** | **2300** |
| **This work** | **-60** | **0.2** | **0.2** | **1370** |

**Table S2. Gutmann donor number.**

| Name | abbreviation | Gutmann donor number kcal mol$^{-1}$ |
|---|---|---|
| **Dimethyl sulfoxide** | **DMSO** | **29.8** |
| 1,3-dimethyl-2-imidazolidinone | DMI | 29 |
| N,N-dimethyl acetamide | DMAC | 27.8 |
| N-methyl-2-pyrrolidone | NMP | 27.3 |
| N,N-dimethyl formamide | DMF | 26.6 |
| 1,2-dimethoxyethane | DME | 24 |
| Trimethyl phosphate | TMP | 23 |
| Tetrahydrofuran | THF | 20 |
| 1,3-dioxolane | DOL | 18 |
| Ethyl acetate | EA | 17.1 |
| Acetone | AC | 17 |
| butyrolactone | GBL | 17 |
| Ethylene carbonate | EC | 16.4 |
| ethylene sulfite | ES | 15.3 |
| Sulfolane | TMS | 14.8 |
| 1,4-Dioxane | DOA | 14.8 |
| Acetonitrile | CAN | 14.1 |
| Benzonitrile | Ph-AC | 11.9 |

Note. Data is originated from Reference (Electrochimica Acta,Volume 21, Issue 9, 1976, Pages 661-670, https://doi.org/10.1016/0013-4686(76)85034-7 )

**Figures**

**Figure S1. Photos of electrolytes**
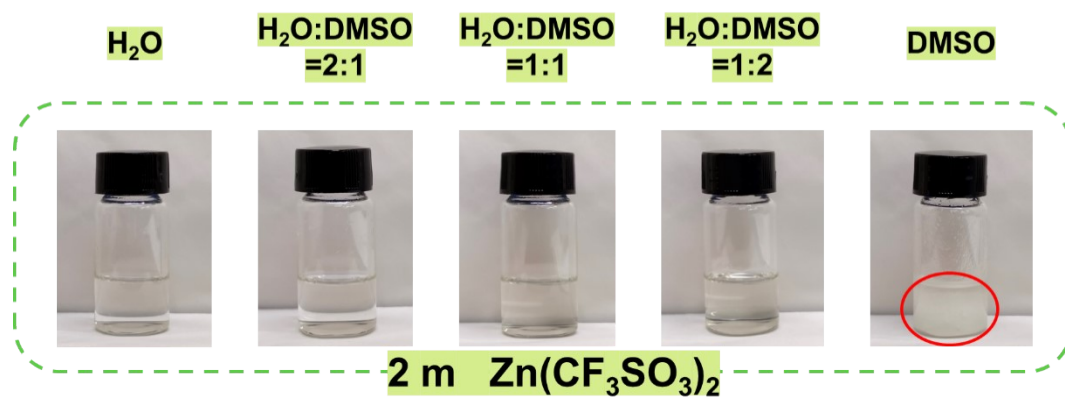


**Fig. S1** Optical photographs of hybrid electrolytes. 2.

$Zn(CF_3SO_3)_2$ is highly soluble in water but insoluble in DMSO, However, DMSO forms a homogenous phase with $Zn(CF_3SO_3)_2$ aqueous electrolytes with the DMSO volume ratio ranging from 33% to 66% due to the good miscibility of DMSO with $H_2O$.

**Figure S2. Flammability test**
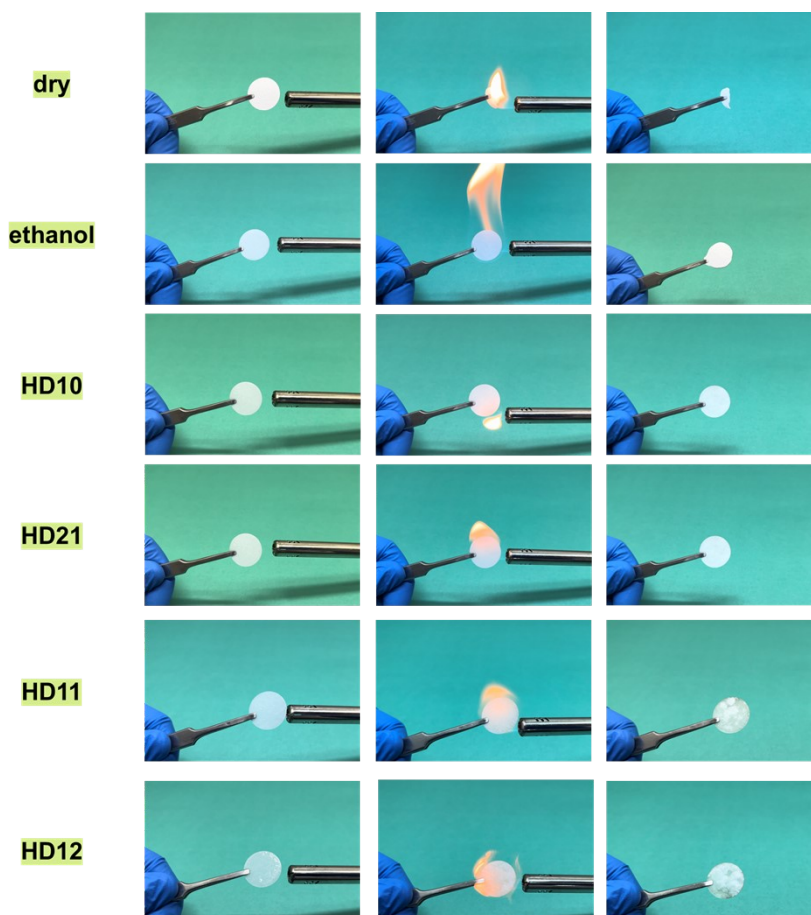


**Fig. S2** Flammability test of hybrid electrolytes.

In addition, the flammability test is carried out by directly igniting the glass fiber disks soaked with the electrolytes to verify the safety. A dry glass fiber shrank immediately. The glass fiber soaked with traditional organic electrolytes such as ethanol is ignited rapidly, which keeps burning after the flame is removed. In contract, the glass fiber soaked with HD21, HD11 and HD12 cannot be ignited. Therefore, the high boiling and flash points of DMSO endow the hybrid electrolytes with high safety for battery applications.

**Figure S3. LSV**
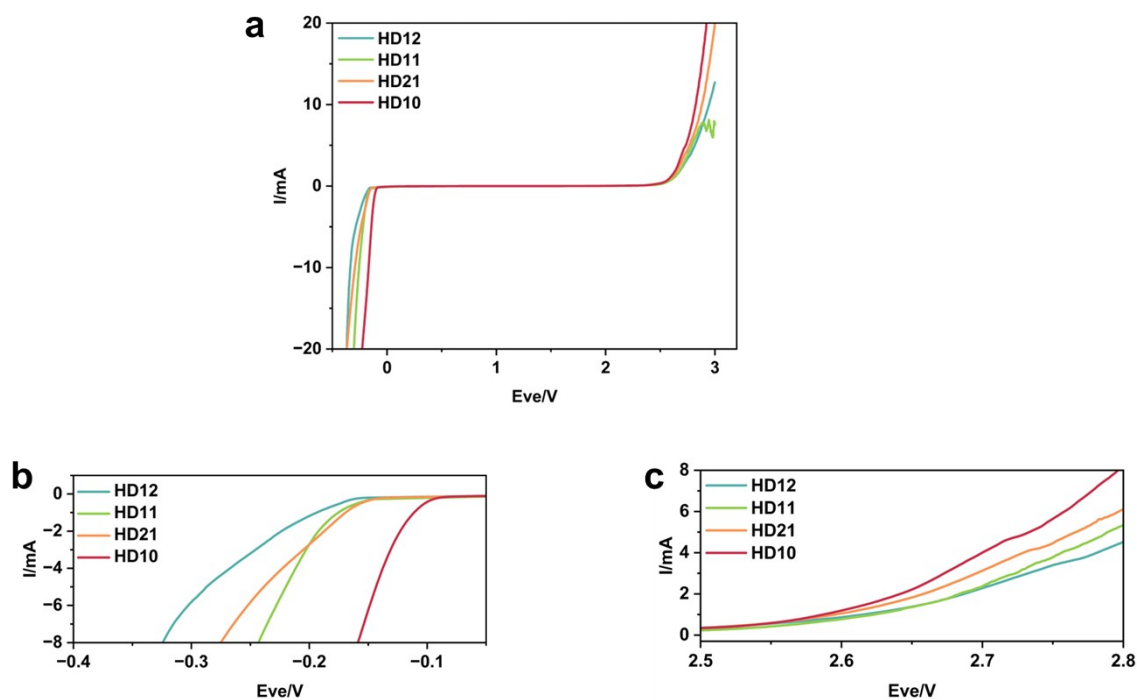


**Fig. S3** Electrochemical stability window of ZFE and hybrid electrolytes measured by linear sweep voltammetry (LSV) and enlarged view of the regions outlined near cathodic and anodic regions.

To unveil the suppression of side reactions upon the addition of DMSO, the electrochemical stability window for these electrolytes is evaluated by using linear sweep voltammetry (LSV) measurements. The presence of DMSO in these electrolytes is found to extend the cathodic limit when compared to the ZFE, which indicates the suppression of hydrogen evolution reaction (HER). In addition, the expanded anodic stability is also observed, and the increased oxygen evolution reaction over-potential further confirms the positive role of the addition of DMSO.

**Figure S4. DSC curves**
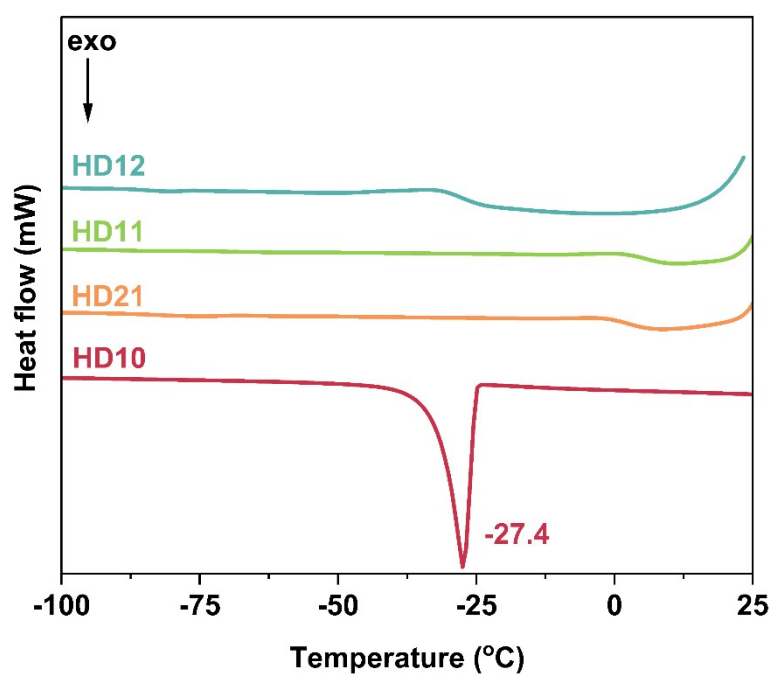


**Fig. S4** DSC curves of ZFE and hybrid electrolytes.

**Figure S5. Frost-resistance test**
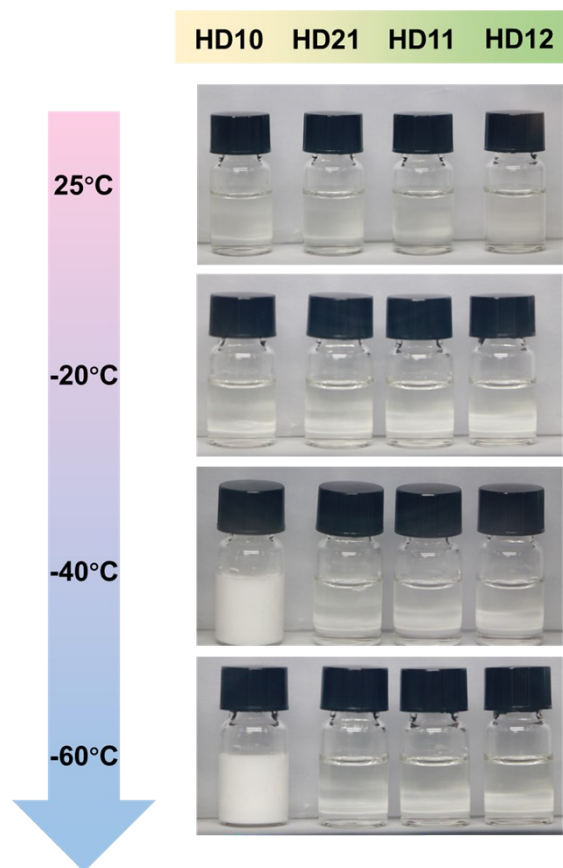


**Fig. S5** Anti-freezing experiments of control electrolyte and hybrid electrolytes at different temperatures.

The anti-freezing capability of hybrid electrolytes with different contents of DMSO is examined. Clearly, no freezing and salt precipitation can be observed when the temperature decreases to -60 °C, indicating the good anti-freezing capability.

**Figure S6. Ion conductivity**
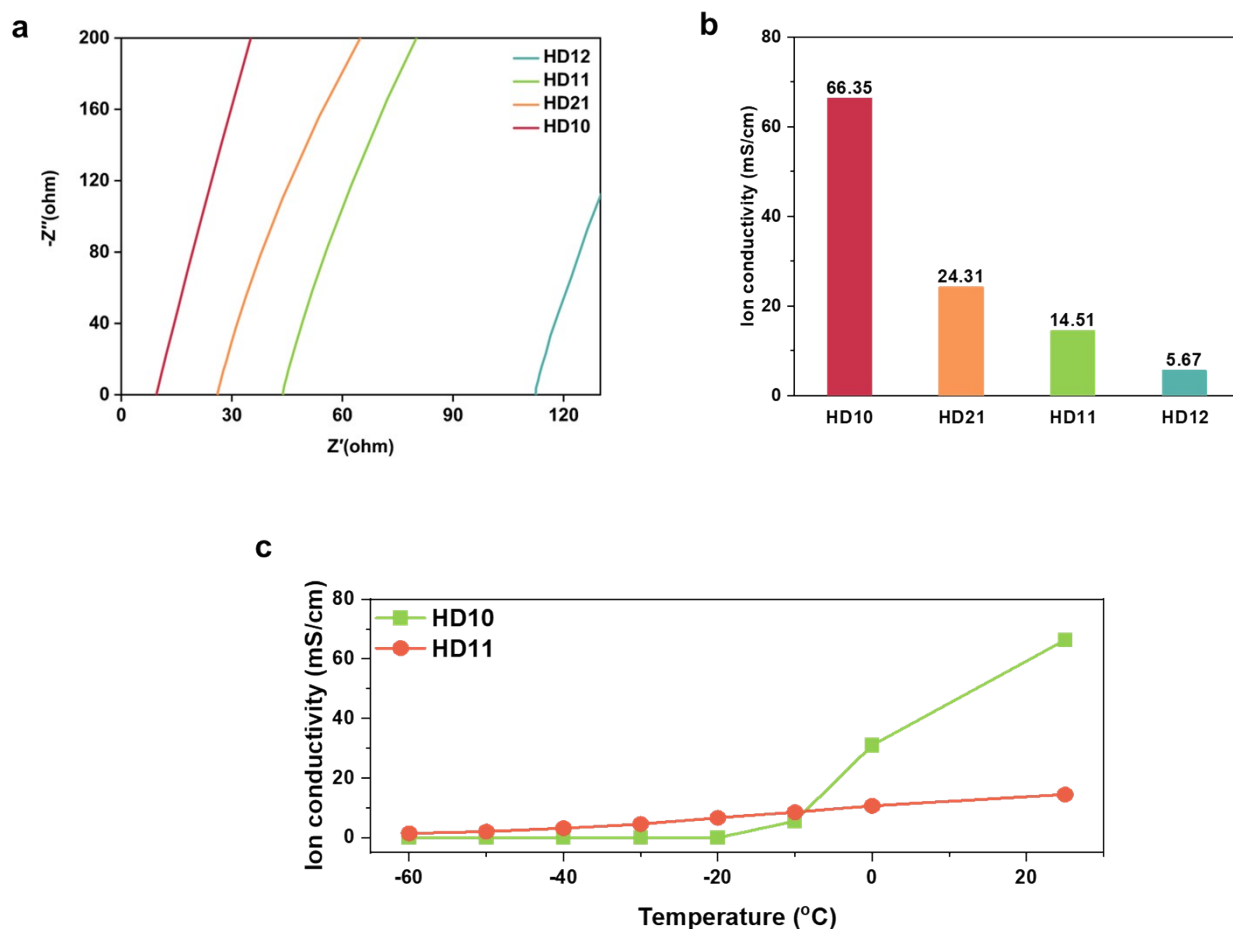


**Fig. S6** Ion conductivity of ZFE and hybrid electrolytes. a) EIS curves; b) Ion conductivity at room temperature; c) Ion conductivity at different temperatures.

The ion conductivity is obtained by the EIS test, which suggests the decreased ion conductivities for hybrid electrolytes due to the increased viscosity. As the temperature drops to -20 °C, HD11 hybrid electrolyte shows much higher ion conductivity than ZFE. At -30 °C, ion conductivity of ZFE drastically decreases to 0 due to the complete freeze, while HD11 hybrid electrolyte maintains high ion conductivity. Even at -60 °C, the ion conductivity is still as high as 1.5 mS·cm$^{-1}$, which affords satisfactory battery performance at ultralow temperature.
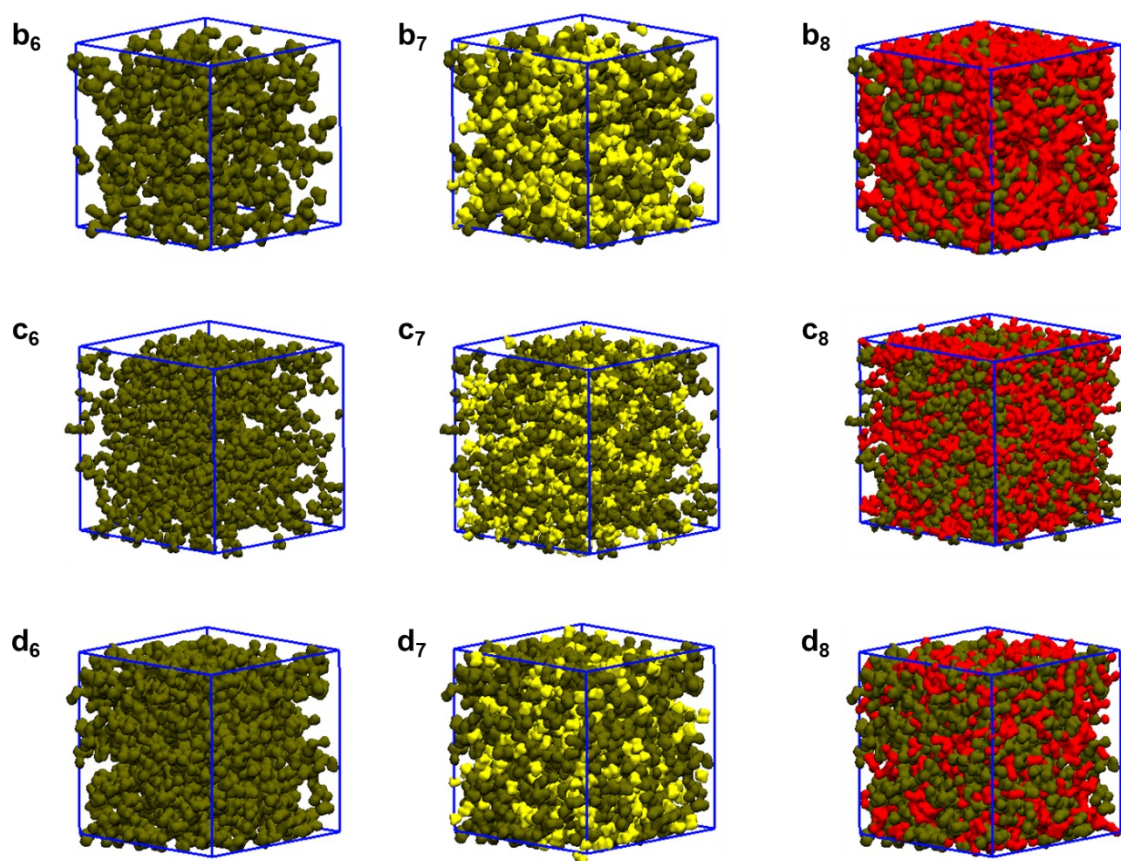
**Figure S7. Nanostruture of ZFE and hybrid electrolytes**
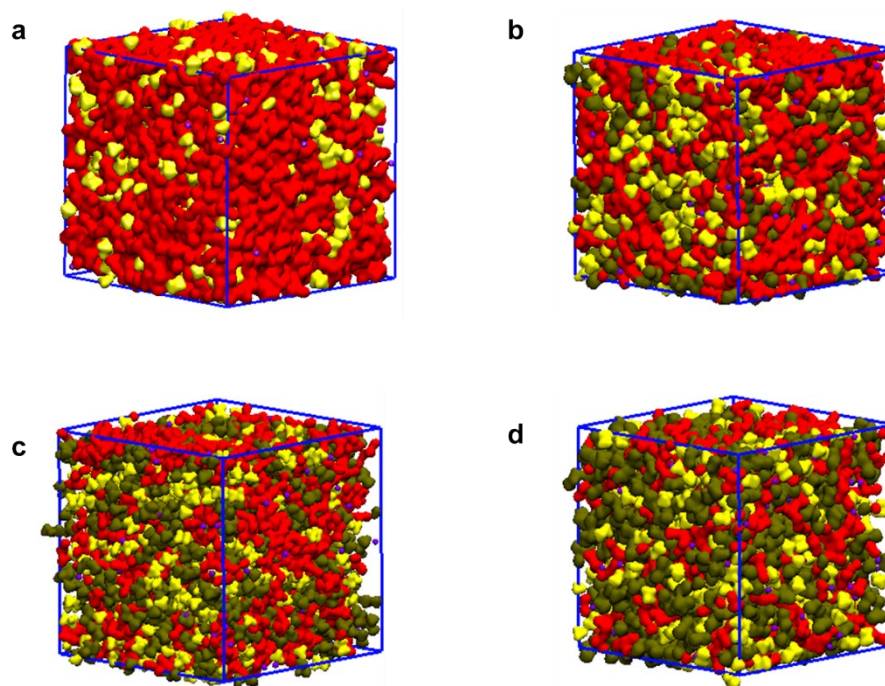


**Fig. S7** Ion or molecule aggregations of ZFE and hybrid electrolytes with different $H_2O$/DMSO volume ratios visualized by molecular dynamics (MD) simulation. a-d) Highlighted snapshot of the MD simulated cell for ZFE (a), HD21 (b), HD11 (c) and HD12 (d). Color bar: $Zn^{2+}$, $CF_3SO_3^-$, DMSO and $H_2O$ are shown in purple, in yellow, in green, and in red, respectively.
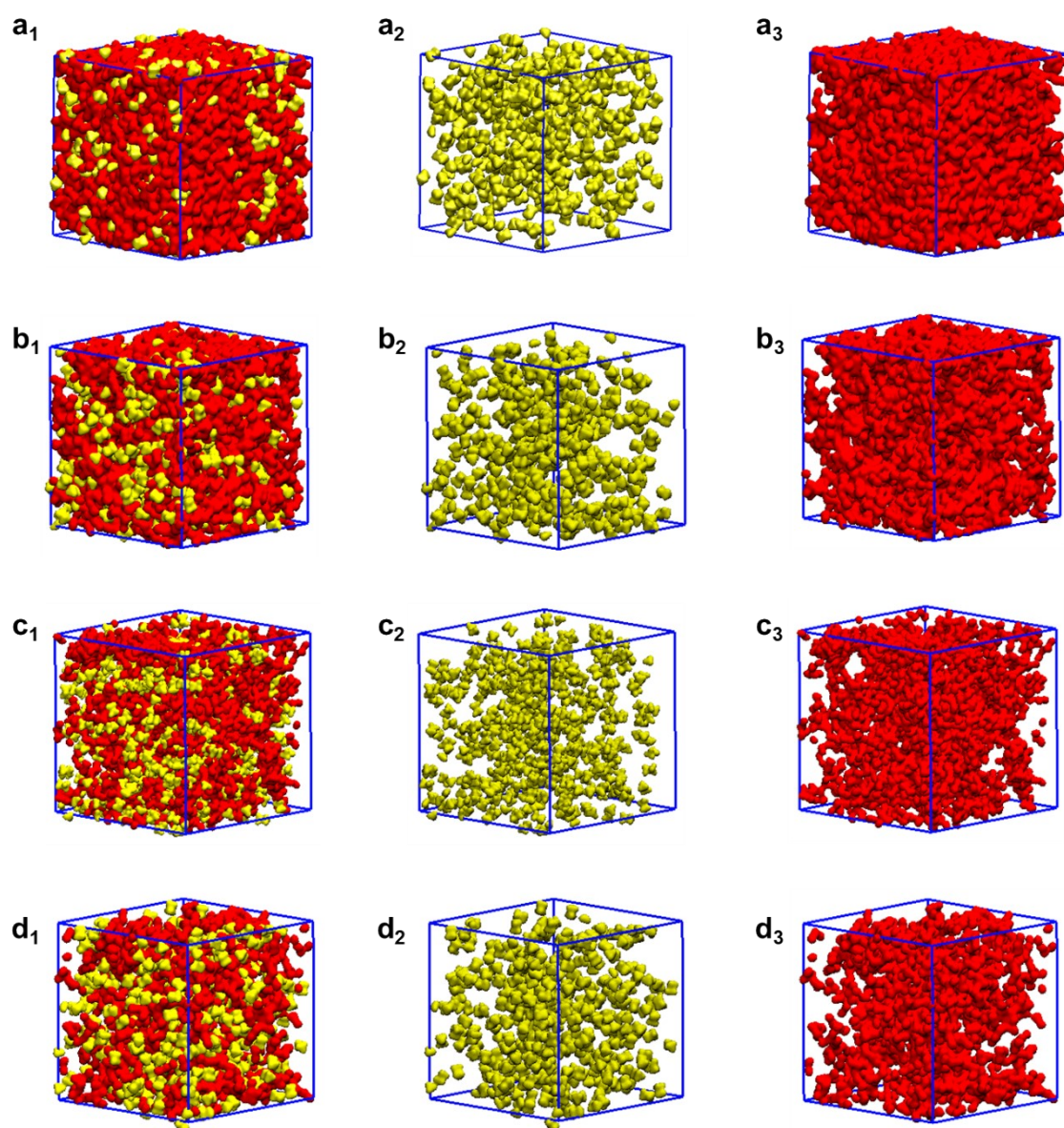
**Fig. S7 Continued.** Ion or molecule aggregations of ZFE and hybrid electrolytes with different $H_2O$/DMSO volume ratios visualized by molecular dynamics (MD) simulation. $a_1$-$d_1$) Highlighted snapshot of the MD simulated cell for $H_2O$ molecules and $CF_3SO_3^-$ to show their spatial aggregations: ZFE ($a_1$), HD21($b_1$), HD11 ($c_1$) and HD12 ($d_1$); $a_2$-$d_2$) Highlighted snapshot of the MD simulated cell for $CF_3SO_3^-$ to show their spatial aggregations: ZFE ($a_2$), HD21($b_2$), HD11 ($c_2$) and HD12 ($d_2$); $a_3$-$d_3$) Highlighted snapshot of the MD simulated cell for $H_2O$ molecules to show their spatial aggregations: ZFE ($a_3$), HD21($b_3$), HD11 ($c_3$) and HD12 ($d_3$). Color bar: $Zn^{2+}$, $CF_3SO_3^-$, DMSO and $H_2O$ are shown in purple, in yellow, in green, and in red, respectively.
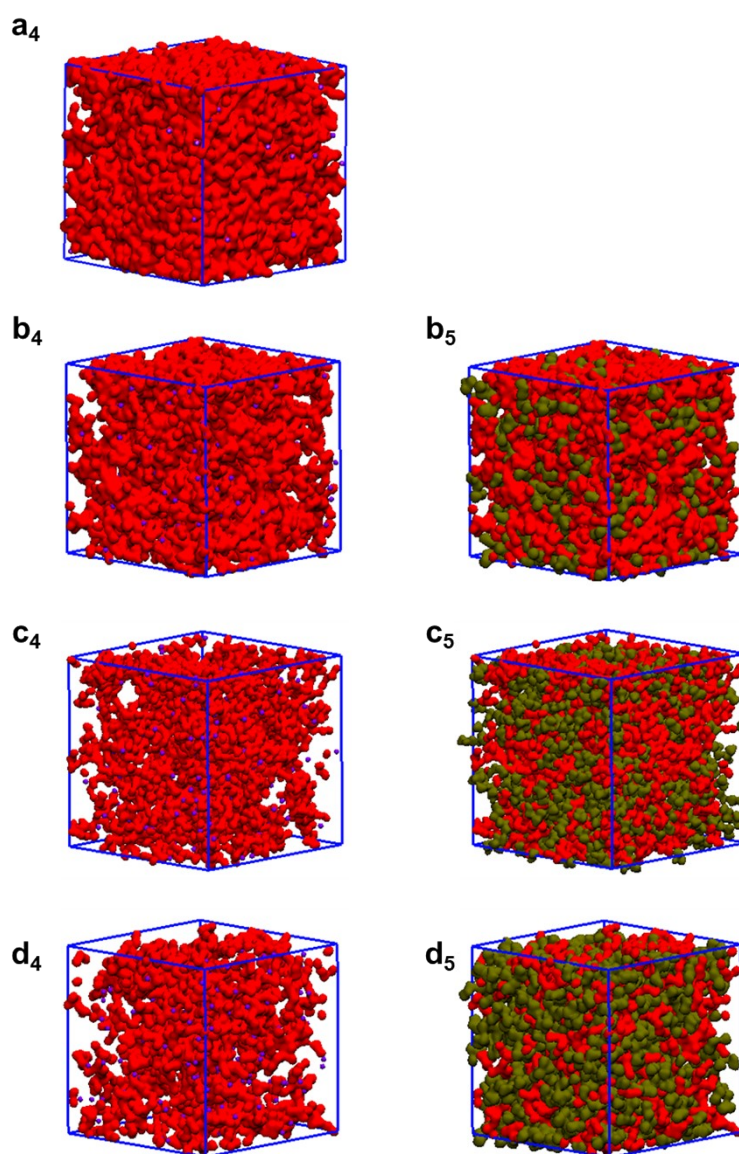
**Fig. S7 Continued.** Ion or molecule aggregations of ZFE and hybrid electrolytes with different $H_2O$/DMSO volume ratios visualized by molecular dynamics (MD) simulation. $a_4$-$d_4$) Highlighted snapshot of the MD simulated cell for $H_2O$ molecules and $Zn^{2+}$ to show their spatial aggregations: ZFE ($a_4$), HD21($b_4$), HD11 ($c_4$) and HD12 ($d_4$); $b_5$-$d_5$) Highlighted snapshot of the MD simulated cell for $H_2O$ molecules and DMSO to show their spatial aggregations: HD21($b_5$), HD11 ($c_5$) and HD12 ($d_5$). Color bar: $Zn^{2+}$, $CF_3SO_3^-$, DMSO and $H_2O$ are shown in purple, in yellow, in green, and in red, respectively.

**Fig. S7 Continued.** Ion or molecule aggregations of ZFE and hybrid electrolytes with different $H_2O$/DMSO volume ratios visualized by molecular dynamics (MD) simulation. $b_6$-$d_6$) Highlighted snapshot of the MD simulated cell for DMSO molecules to show their spatial aggregations: HD21 ($b_6$), HD11 ($c_6$) and HD12 ($d_6$); $b_7$-$d_7$) Highlighted snapshot of the MD simulated cell for DMSO molecules and $CF_3SO_3^-$ to show their spatial aggregations: HD21 ($b_7$), HD11 ($c_7$) and HD12 ($d_7$); $b_8$-$d_8$) Highlighted snapshot of the MD simulated cell for DMSO and $H_2O$ molecules to show their spatial aggregations: HD21 ($b_8$), HD11 ($c_8$) and HD12 ($d_8$). Color bar: $Zn^{2+}$, $CF_3SO_3^-$, DMSO and $H_2O$ are shown in purple, in yellow, in green, and in red, respectively.

**Figure S8. Isosurface images for ion and molecule of electrolytes**
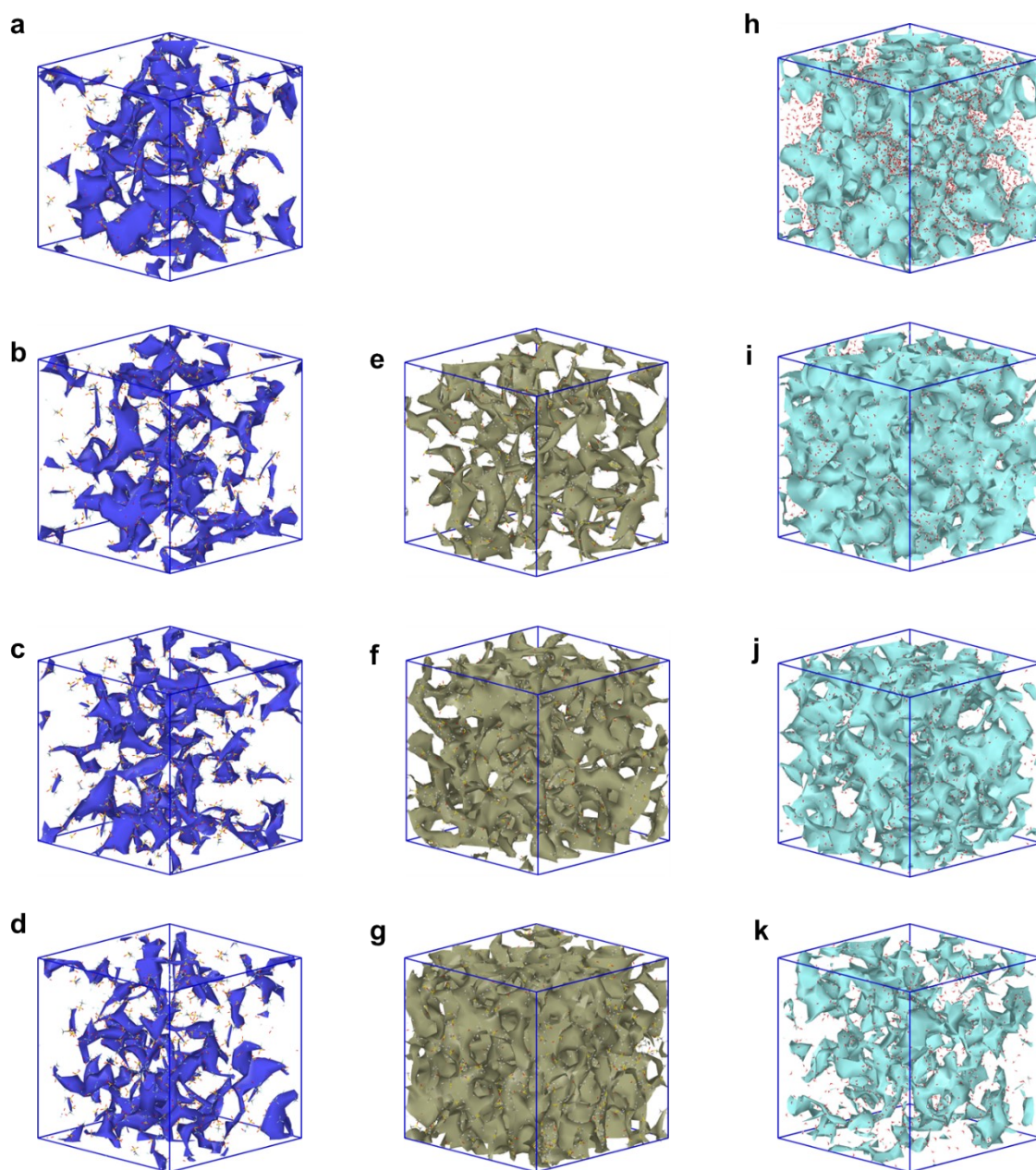


**Fig. S8** Isosurface images for ion and molecule of ZFE and hybrid electrolytes visualized by molecular dynamics (MD) simulation. a-d) Isosurface images for $CF_3SO_3^-$ anions: ZFE (a), HD21 (b), HD11 (c) and HD12 (d); e-g) Isosurface images for DMSO molecules: HD21 (e), HD11 (f) and HD12 (g); h-k) Isosurface images for $H_2O$ molecules: ZFE (h), HD21, (i), HD11, (j) and HD12 (k).

**Figure S9. Calculating Zn²⁺ transference number based on CA tests**
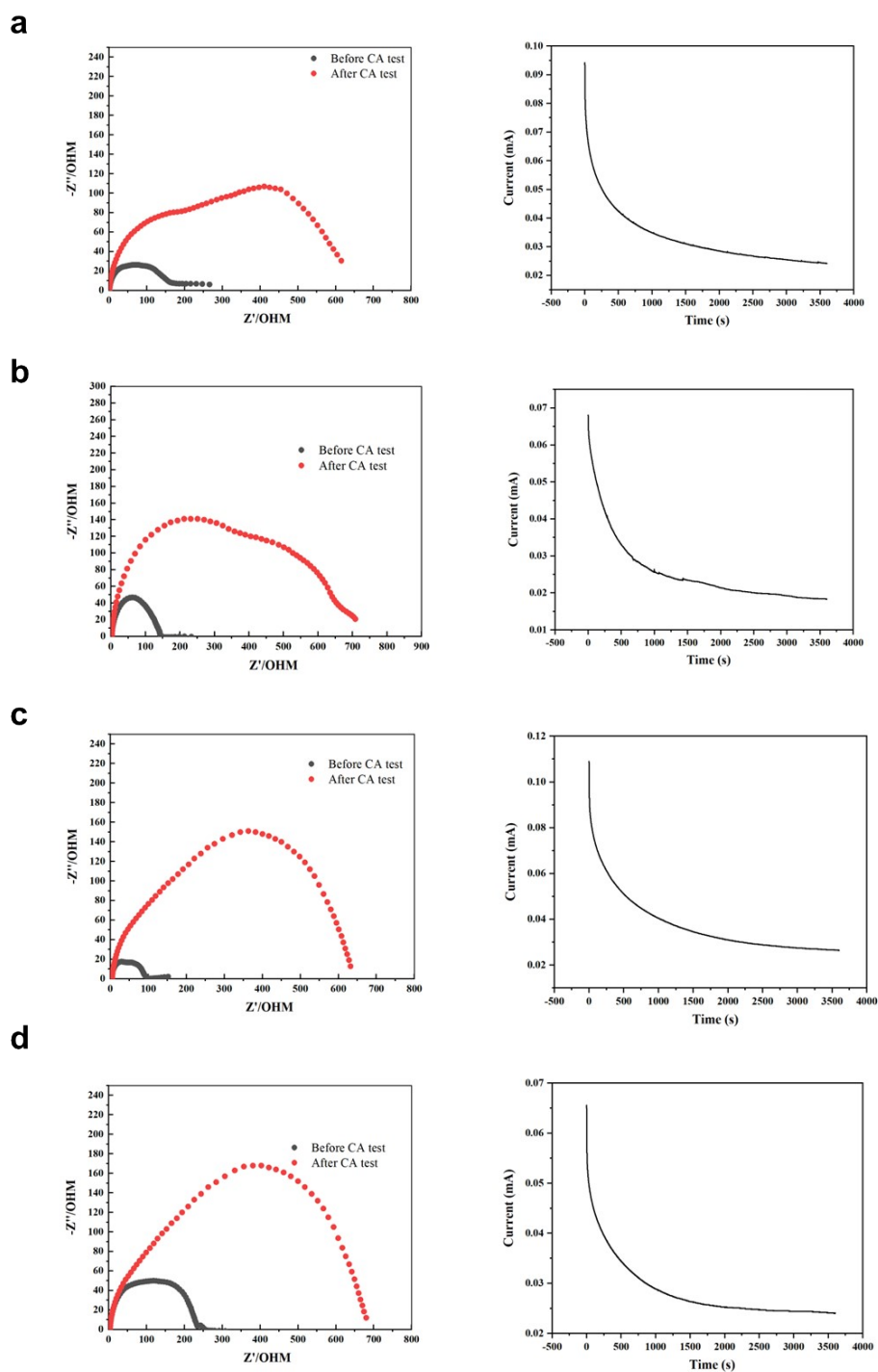


**Fig. S9** CA curves (left) and Nyquist plots (right) for symmetric cells before and after polarization: ZFE (a), HD21 hybrid electrolyte (b), HD11 hybrid electrolyte (c) and HD12 hybrid electrolyte (d).

**Figure S10. Calculating Ea based on temperature-dependent EIS.**
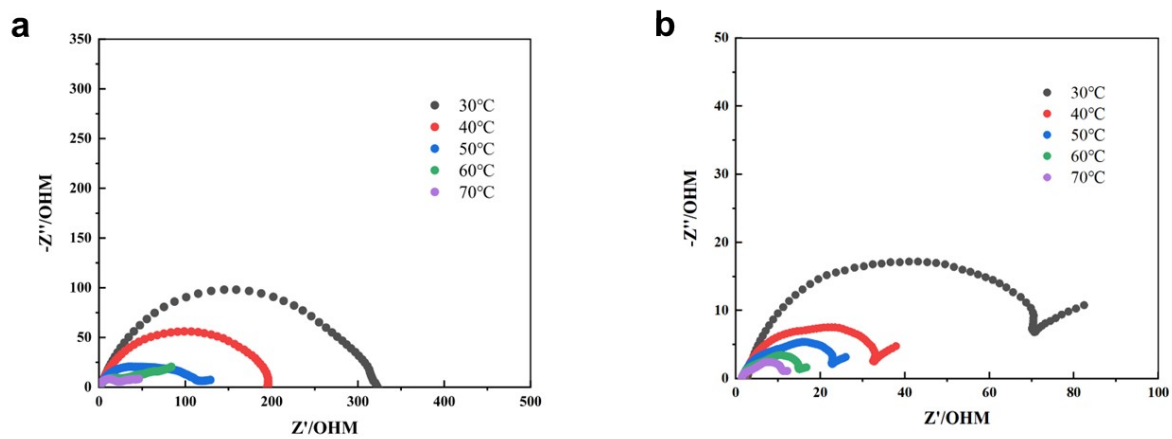


**Fig. S10** Nyquist plots at different temperatures of ZFE (a) and HD11 hybrid electrolyte (b).

**Figure S11. DFT calculation for electrostatic potential mapping**
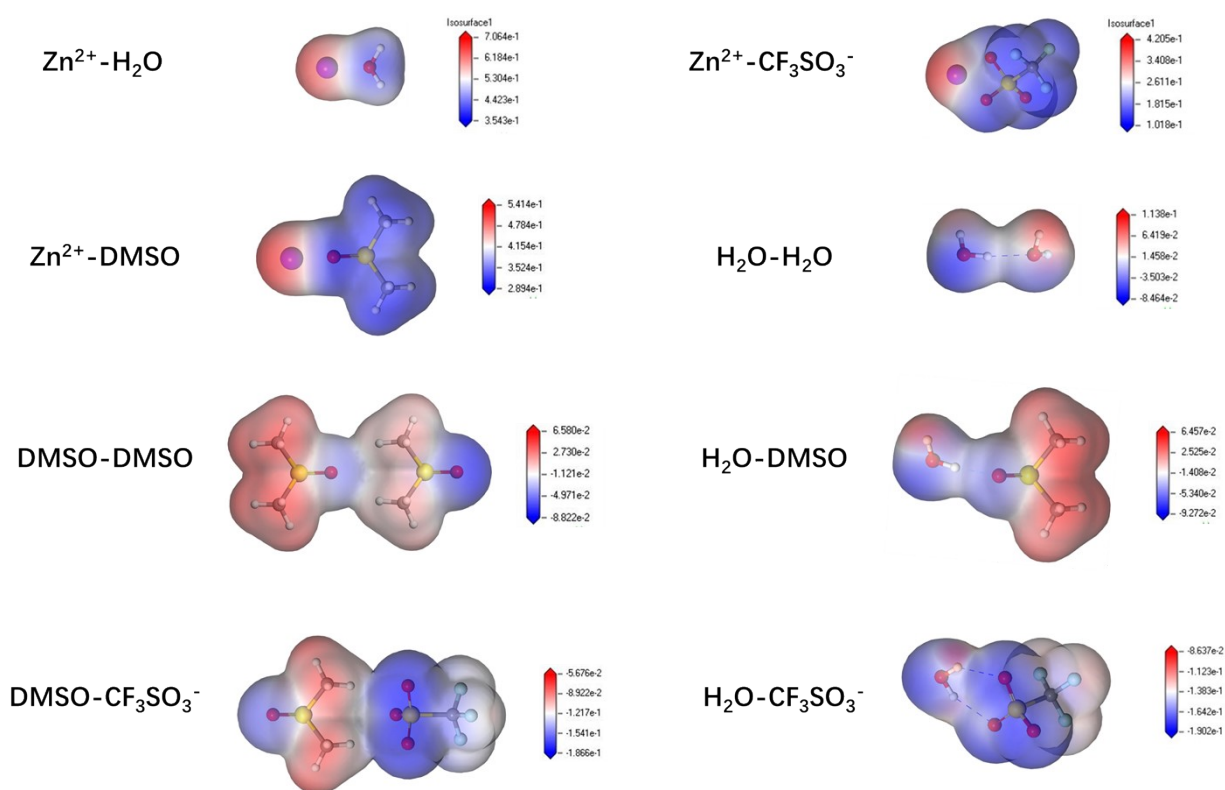


**Fig. S11** Electrostatic potential mapping clearly showed the charge distribution of any two constituents in the hybrid electrolytes.
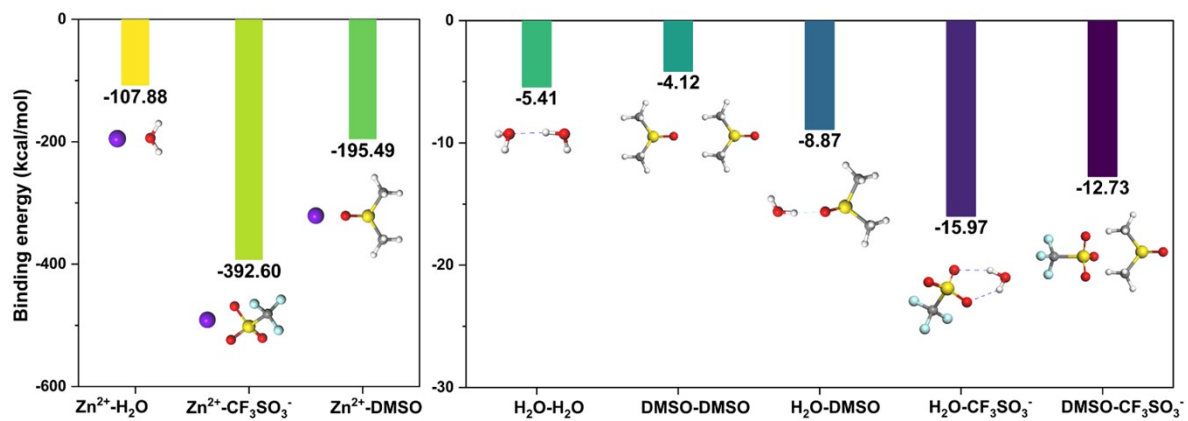
**Fig. S11 Continued.** Binding energy of any two constituents in the hybrid electrolytes.

**Figure S12. ^{1}HNMR spectra**
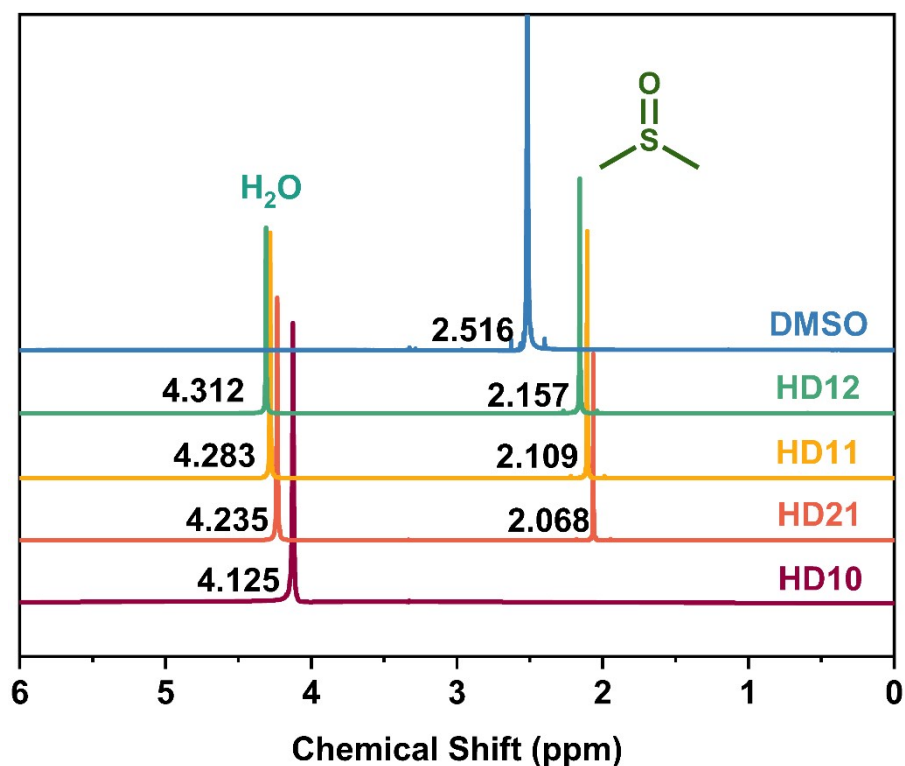


**Fig. S12** [1]H nuclear magnetic resonance (^{1}H NMR) spectroscopy of ZFE, hybrid electrolytes and pure DMSO solvent at room temperature.

As can be seen from the ^{1}H NMR spectra, the chemical shift at 4.125 ppm is attributed to the hydrogen proton in water and the chemical shift at 2.516 ppm corresponds to the methyl group in DMSO. After the introduction of DMSO in the electrolyte, a significant shift is observed with both two chemical shifts of OH and $CH_3$ groups, indicating the hydrogen bond is restructured and the new hydrogen bond is formed between water and DMSO. The chemical shifts of methyl group are much lower than that in DMSO, which further illustrating hydrogen bond network between DMSO and $H_2O$. As the concentration of DMSO increase, the chemical shift of methyl group increases from 2.068 ppm to 2.157 ppm, demonstrating the hydrogen bond is enhanced. At the same time, the chemical shift of hydrogen proton also moves to downfield from 4.235 ppm to 4.312 ppm, which proves that the hydrogen bond between water and DMSO is stronger than that in water.

**Figure S13. $^{19}$FNMR spectra**
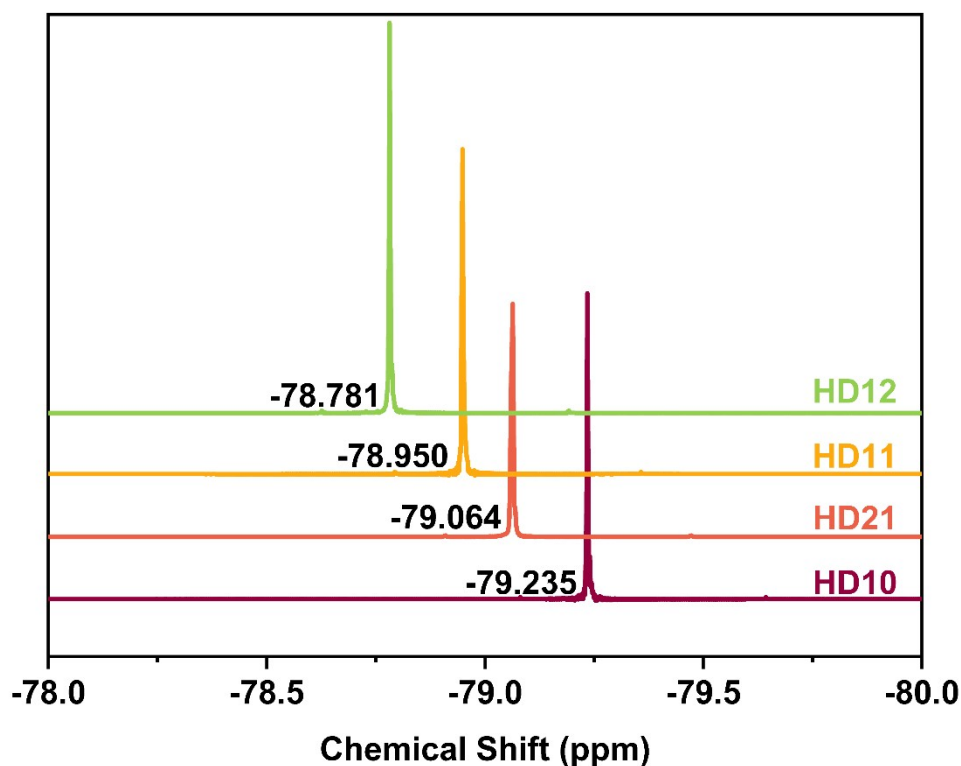


**Fig. S13** $^{19}$F nuclear magnetic resonance ($^{19}$F NMR) spectroscopy of ZFE and hybrid electrolytes at room temperature.

$^{19}$F NMR spectra are also detected to assign the presence of anions in the $Zn^{2+}$ solvation sheath. In the ZFE, the chemical shift of $CF_3SO_3^-$ anion appears at -79.235 ppm. $^{19}$F NMR spectra of hybrid electrolytes undergo a downfield-shift from-79.235 ppm to -78.781 ppm along with the increase of DMSO concentration, indicating the improved de-shielding effect of the $CF_3SO_3^-$ anion and the enhanced interaction between $CF_3SO_3^-$ anion and $Zn^{2+}$, which creates the access for $CF_3SO_3^-$ anions to enter the $Zn^{2+}$ solvation sheath in the hybrid electrolytes.

**Figure S14. ¹HNMR spectra at different temperatures**
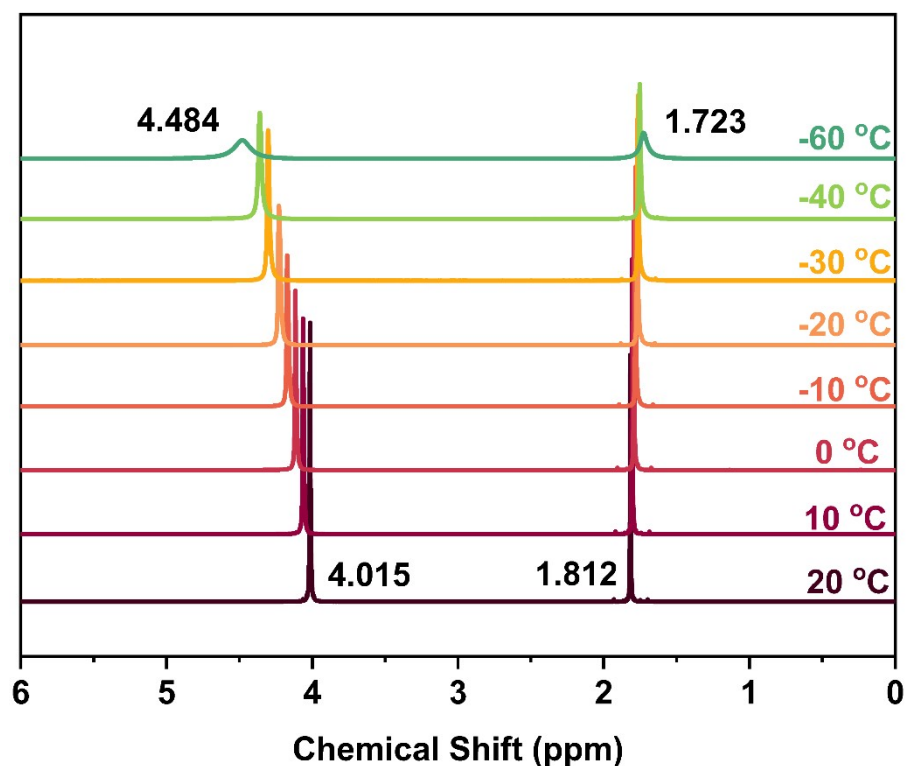


**Fig. S14** $^1$H nuclear magnetic resonance ($^1$H NMR) spectroscopy of of HD11 electrolyte at different temperatures.

Moreover, the $^1$H NMR spectra of HD11 electrolyte at variable temperatures was detected to study the solvation interaction at low temperatures. The chemical shift of hydrogen proton in water and methyl group in DMSO appear at 4.015 ppm and 1.812 ppm at 20 ℃, respectively. As the temperature decrease, the peak width of OH and $CH_3$ groups increases, but peak intensity decreases gradually, which convincingly proves the restricted molecule motility and the enhanced molecule association. When the temperature decreases to -60 ℃, the chemical shift of the hydrogen proton increases to 4.484 ppm. While the chemical shift of the methyl group decreases from 1.812 ppm to 1.723 ppm. This can be attributed to the fact that the stronger hydrogen bond interactions at low temperature.
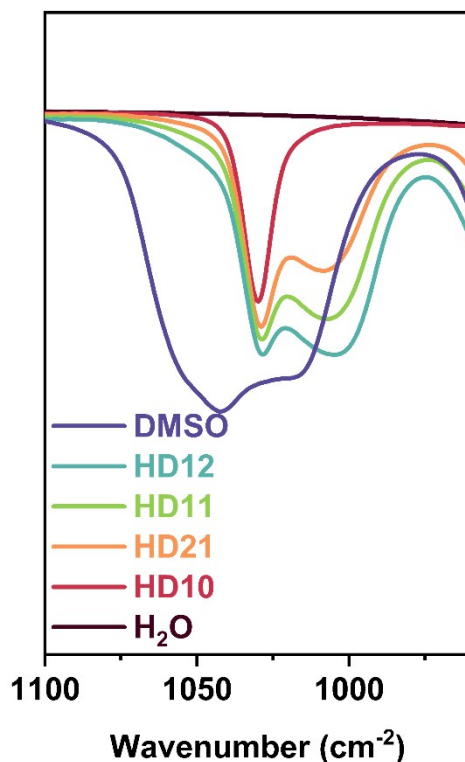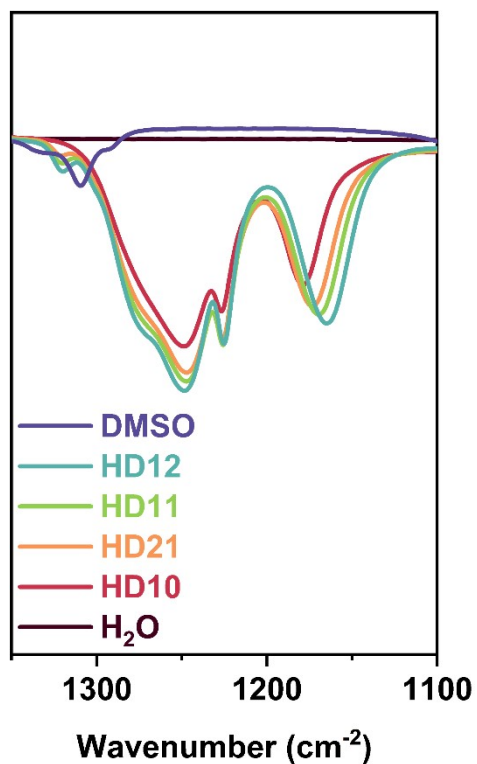
**Figure S15. ATR-FTIR spectra**
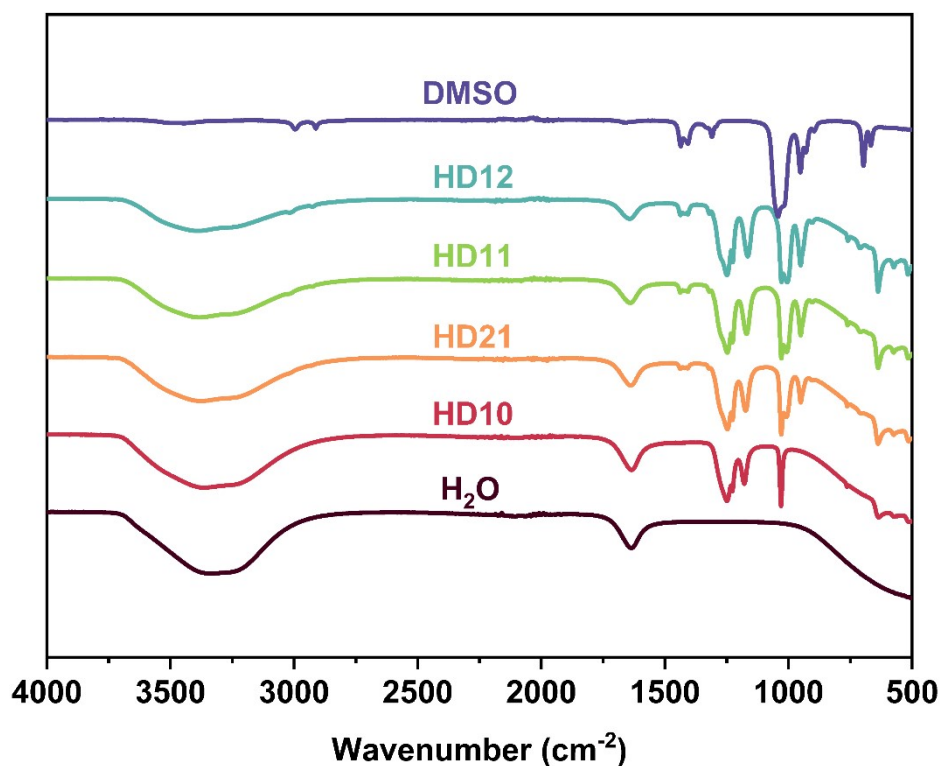


**Fig. S15** Attenuated total reflectance Fourier transform infrared (ATR-FTIR) spectra of ZFE and hybrid electrolytes.

The strong interaction in hybrid electrolytes are demonstrated by ATR-FTIR. The bands located in 3000-3700 cm$^{-1}$ and around 1640 cm$^{-1}$ correspond to O-H stretching vibration and O-H bending vibration in water, respectively. The bands appearing around 1040 cm$^{-1}$ and 1007 cm$^{-1}$ are assigned to S=O stretching vibration. The bands in the region of 1240-1270 cm$^{-1}$ and at around 1027 cm$^{-1}$ are ascribed to the antisymmetric and symmetric SO$_3$ stretching vibration, while the bands located in 1150-1180 cm$^{-1}$ and 1220-1230 cm$^{-1}$ are the symmetric and antisymmetric CF$_3$ stretching vibration, respectively.
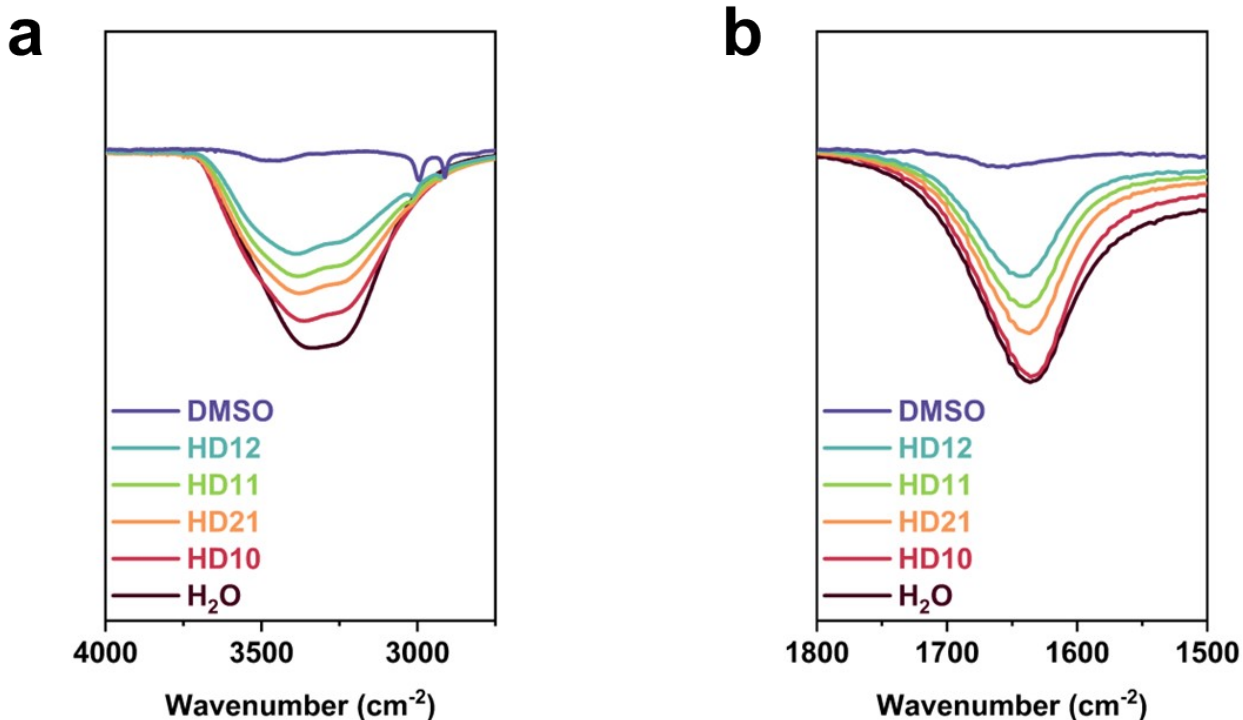
**Fig. S15 Continued.** Attenuated total reflectance Fourier transform infrared (ATR-FTIR) spectra of ZFE and hybrid electrolytes in OH bending vibration and stretching vibration region.

The O-H stretching vibration band of pure water appears at 3335 cm$^{-1}$, and it show a blue-shift to 3363 cm$^{-1}$ with the introduction of $Zn(CF_3SO_3)_2$, indicating some of the water enters the coordination sphere of $Zn^{2+}$ and the hydrogen bond interactions within the water is weakened. When DMSO is added in the electrolyte, the O-H stretching vibration band shows the unignorable blue shifts, implying the hydrogen bond interactions of water molecules become weaker in hybrid electrolytes.

**Fig. S15 Continued.** Attenuated total reflectance Fourier transform infrared (ATR-FTIR) spectra of ZFE and hybrid electrolytes in S=O stretching vibration region.

The S=O stretching vibration band of hybrid electrolytes show a dramatic red-shift compared with that in pure DMSO, indicating the dipole-dipole interactions between DMSO molecules are replaced by hydrogen bond interactions between H of the O-H bond in water molecules and O of the S=O double bond in DMSO, and the hydrogen bond interaction is expected to be stronger than the dipole-dipole interaction. As the increase of the DMSO concentration, the bands move to lower wavenumbers, illustrating more DMSO molecules participate the information of the S=O…H-O hydrogen bond.

**Fig. S15 Continued.** Attenuated total reflectance Fourier transform infrared (ATR-FTIR) spectra of ZFE and hybrid electrolytes in OH stretching vibration region.

There is the opposite shift for $SO_3$ stretching vibration (blue-shift) and $CF_3$ stretching vibration (red-shift), upon the gradually addition of DMSO in the electrolytes, further revealing the enhanced interactions between $Zn^{2+}$ and $CF_3SO_3^-$ anion.

**Figure S16. Raman spectra**
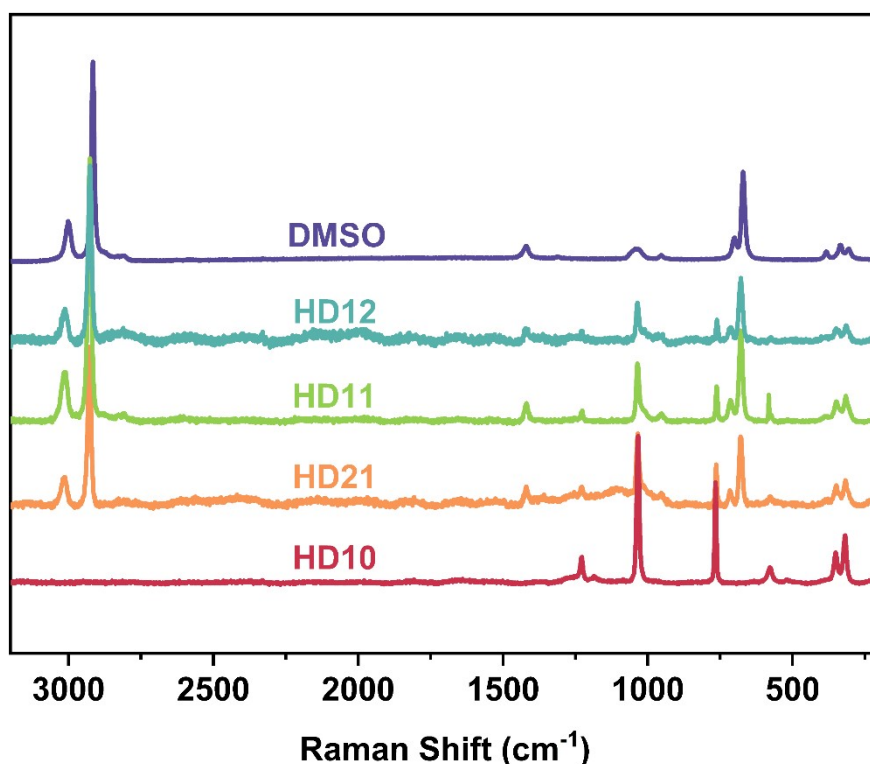


**Fig. S16** Raman spectra of ZFE and hybrid electrolytes.

The OH stretching band of $H_2O$ between 3400 to 3600 cm$^{-1}$ shifts to lower wavenumbers with the increase of DMSO, indicating that more or stronger hydrogen bonds have been formed between DMSO and $H_2O$.

At the same time, the symmetric and asymmetric stretching vibration bands of $CH_3$ in pure DMSO appear at 3001 and 2916 cm$^{-1}$. Regarding to Zn-DMSO ($Zn(CF_3SO_3)_2$ is dissolved in pure DMSO), symmetric and asymmetric stretching vibration bands of $CH_3$ move to higher wavenumber, indicating the interactions between $Zn^{2+}$ and DMSO. As for the hybrid electrolytes, symmetric and asymmetric stretching vibration bands of $CH_3$ continue to exhibit blue shifts, which is due to the reduced density of the electron cloud of $CH_3$ caused by the strong hydrogen bond interactions between S=O and $H_2O$ as well as the interactions between $Zn^{2+}$ and DMSO.

In addition, Raman spectra show two bands between 660 to 720 cm$^{-1}$ ascribed to the C-S symmetric and asymmetric stretching modes of DMSO. After the introduction of DMSO in the electrolytes, these bands gradually shifted to higher wavenumber, indicating a transition from free DMSO to $Zn^{2+}$-solvated DMSO complexes, which further proves that DMSO remodels the solvation structure.

The peaks at around 1030 cm$^{-1}$ are composed of two parts, including the S=O vibration band of DMSO and the -SO$_3$ stretching vibration of CF$_3$SO$_3^-$ anions. In the hybrid electrolytes, the weak S=O vibration band is obscured by the strong -SO$_3$ stretching vibration peak, and as the DMSO concentration increases, the -SO$_3$ stretching vibration peak shifts to higher wavenumbers. This can be explained that the free anions reduce and the aggregated ion cluster increase, implying more CF$_3$SO$_3^-$ anions enter the Zn$^{2+}$ solvation shell. With the increase of DMSO content in the solvent, the interaction between Zn$^{2+}$ and CF$_3$SO$_3^-$ is enhanced, and CF$_3$SO$_3^-$ is forced to participate in the Zn$^{2+}$ solvated shells. The enhanced interaction between Zn$^{2+}$ and CF$_3$SO$_3^-$ is also evidenced by the red shifts of CF$_3$ stretching vibration.
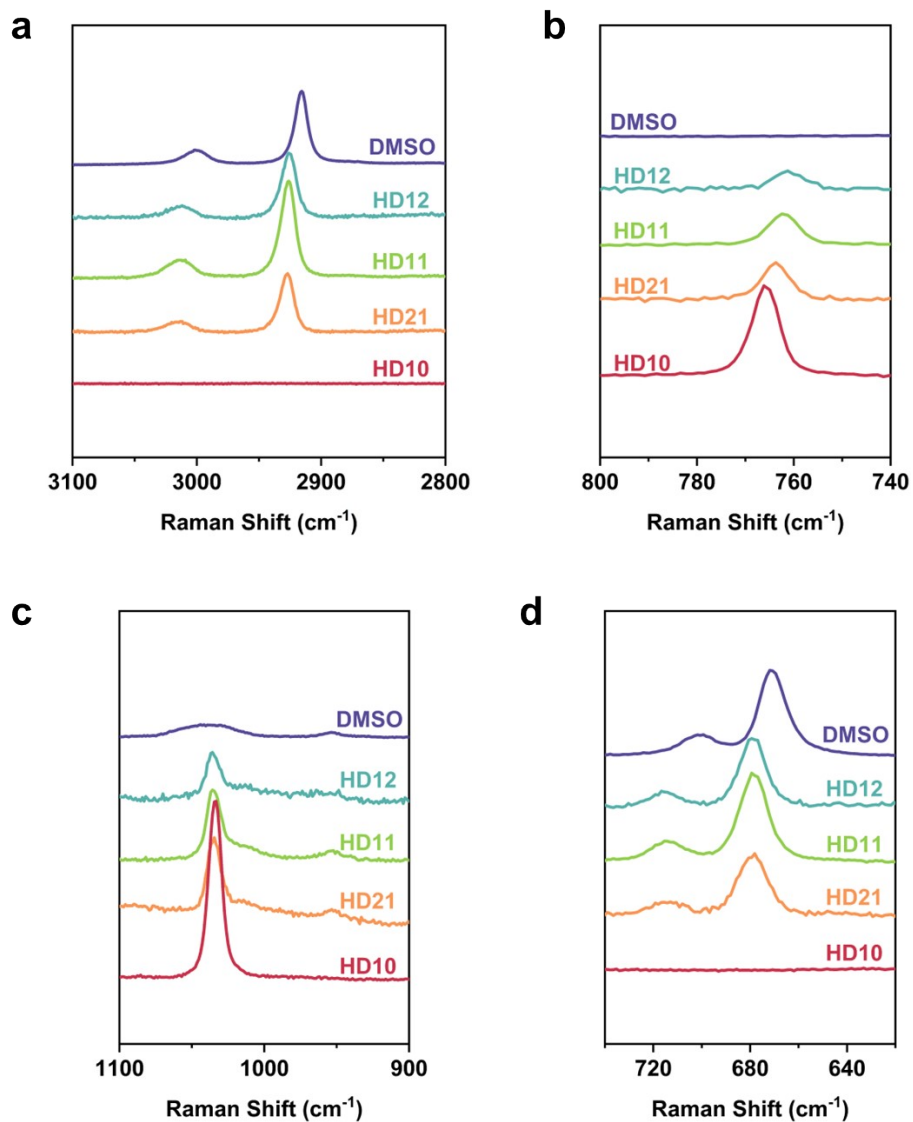
**Fig. S16 Continued.** Raman spectra of ZFE and hybrid electrolytes. a) $CH_3$ stretching vibration region; b) C-S stretching vibration region of DMSO; c) S=O and $SO_3^-$ stretching vibration region; d) $CF_3$ stretching vibration region of $CF_3SO_3^-$.

**Figure S17. XANES spectra**
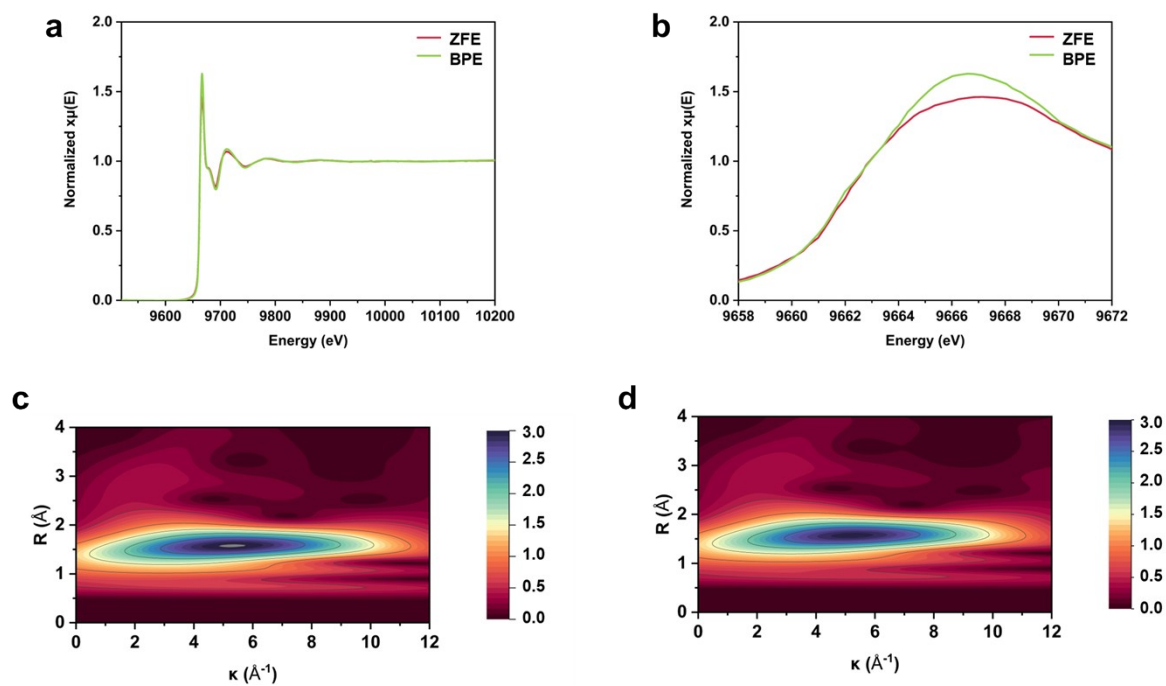


**Fig. S17** Zn K-edge X-ray absorption near-edge structure (XANES) spectra of ZFE and BPE. a) The normalized XANES spectra; b) The local enlarged XANES spectra. The corresponding Wavelet transform images of the EXAFS spectra for c) ZFE and d) BPE.

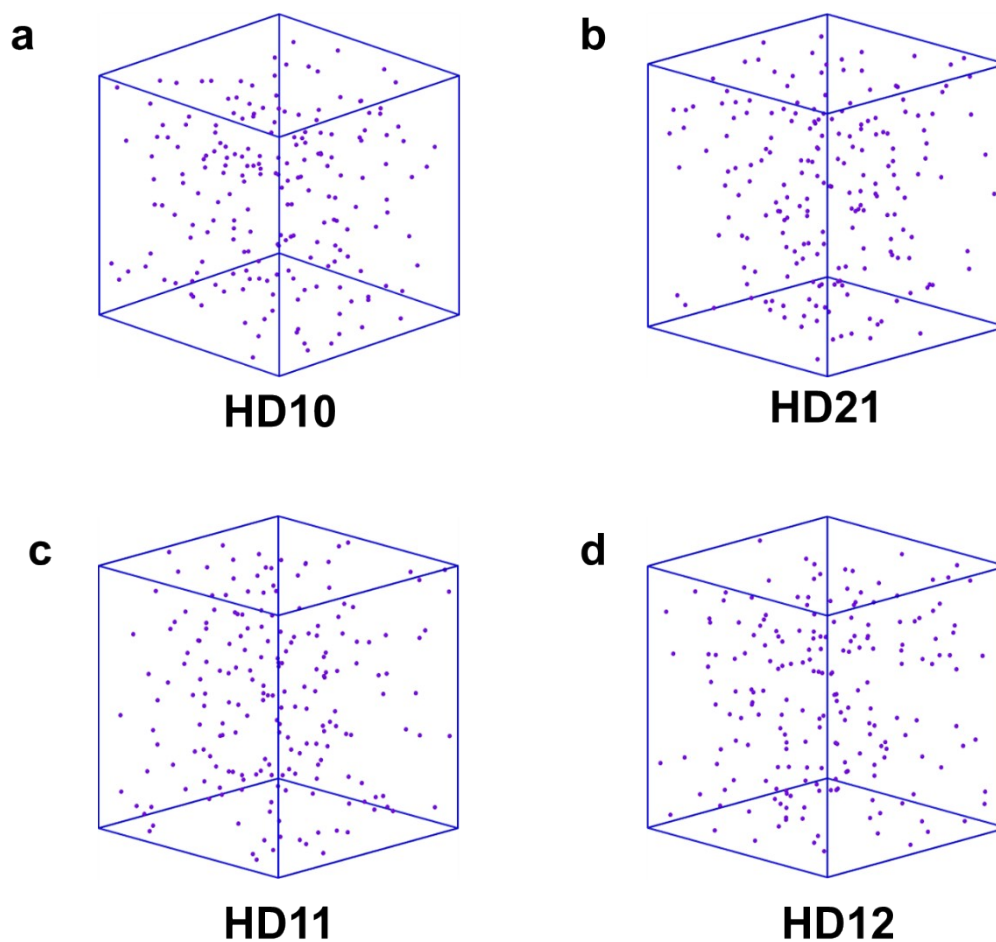**Figure S18. Molecular dynamics (MD) simulation for electrolyte structure**
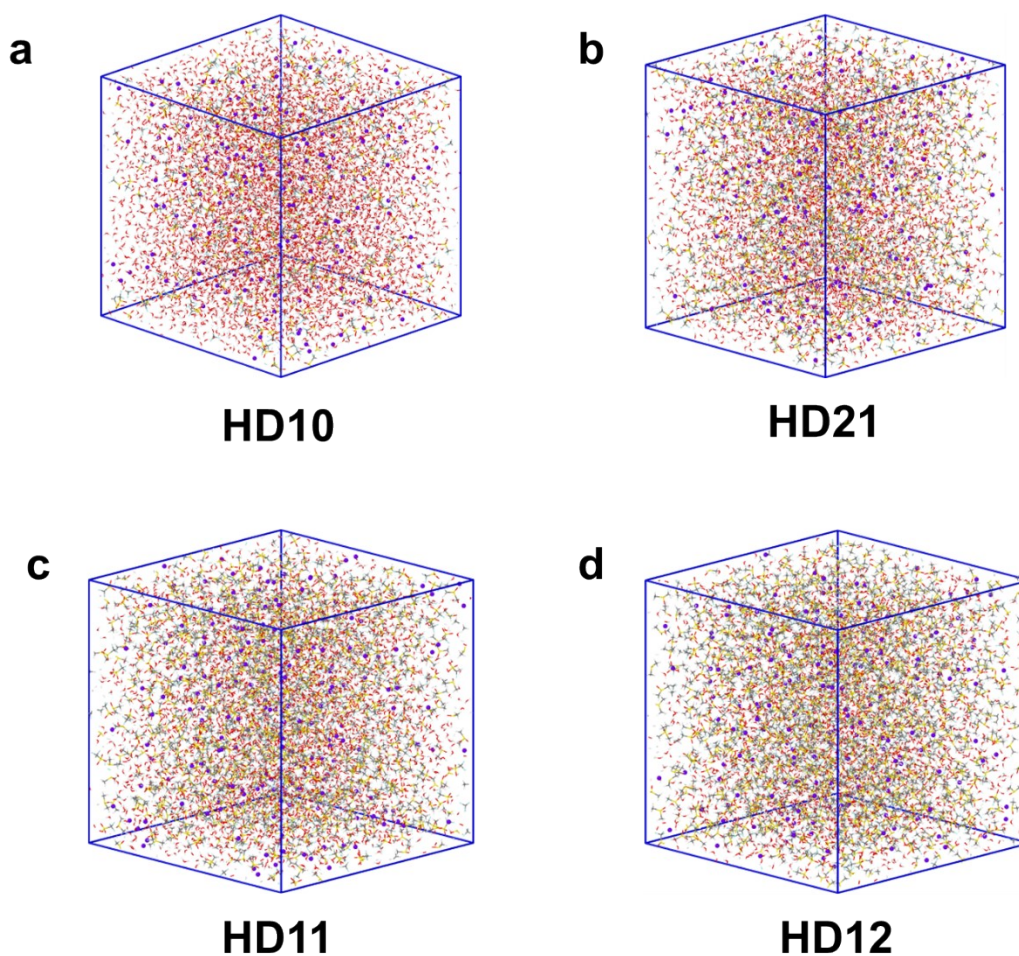


**Fig. S18** Structure of hybrid electrolytes with different $H_2O$/DMSO volume ratios visualized by molecular dynamics (MD) simulation. a) Snapshot of the MD simulated cell for ZFE; b) Snapshot of the MD simulated cell for HD21; c) Snapshot of the MD simulated cell for HD11; d) Snapshot of the MD simulated cell for HD12. The molecules are depicted by ball and stick model, and the zinc, carbon, hydrogen, oxygen, sulfur and fluorine atoms are shown in purple, in gray, in white, in red, in yellow and in blue, respectively.
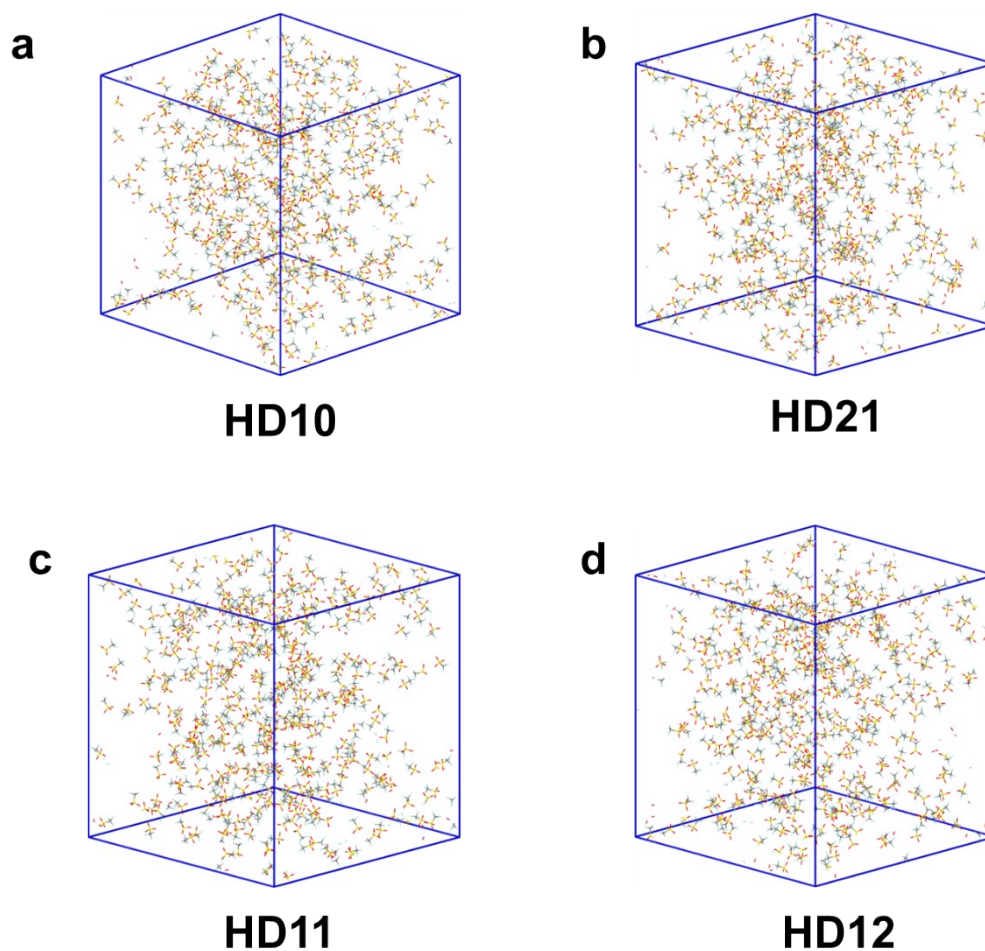
**Fig. S18 Continued.** Structure of hybrid electrolytes with different $H_2O$/DMSO volume ratios visualized by molecular dynamics (MD) simulation to highlight $CF_3SO_3^-$ distribution. a) Snapshot of the MD simulated cell for ZFE; b) Snapshot of the MD simulated cell for HD21; c) Snapshot of the MD simulated cell for HD11; d) Snapshot of the MD simulated cell for HD12. The molecules are depicted by ball and stick model, and the carbon, oxygen, sulfur and fluorine atoms are shown in gray, in red, in yellow and in blue, respectively.
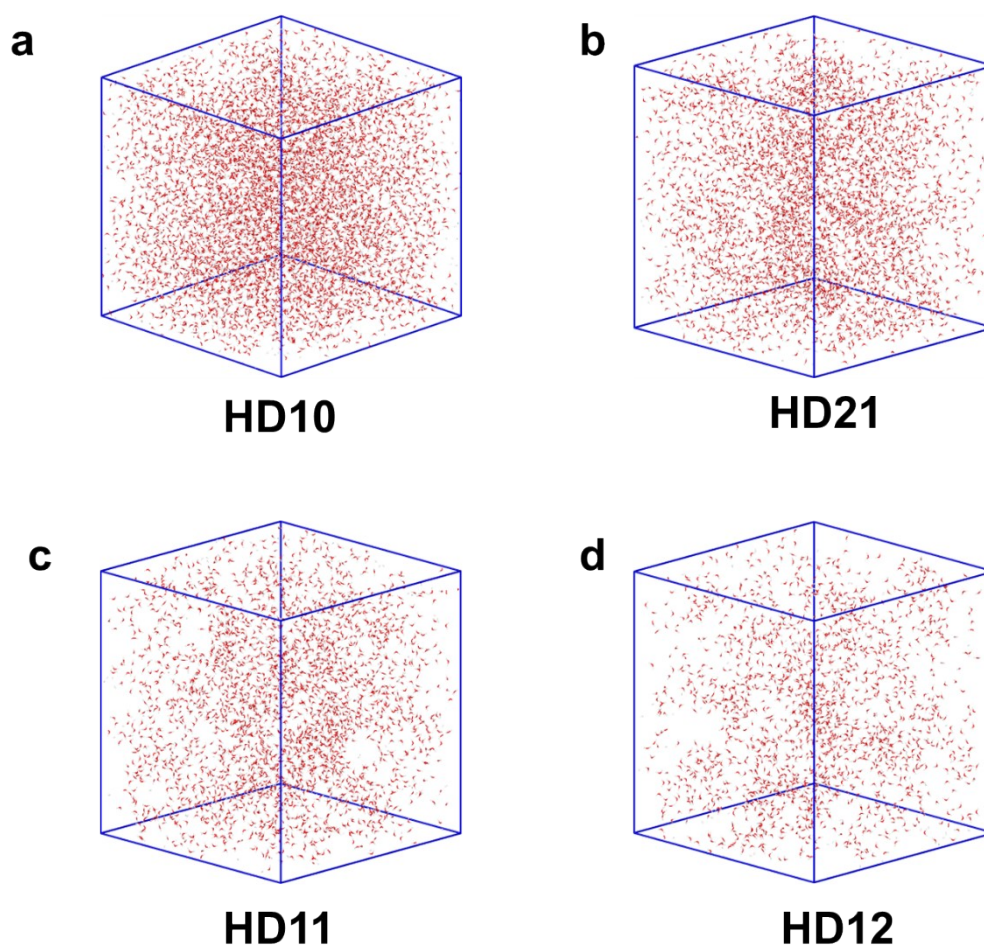
**Fig. S18 Continued.** Structure of hybrid electrolytes with different $H_2O$/DMSO volume ratios visualized by molecular dynamics (MD) simulation to highlight $H_2O$ distribution. a) Snapshot of the MD simulated cell for ZFE; b) Snapshot of the MD simulated cell for HD21; c) Snapshot of the MD simulated cell for HD11; d) Snapshot of the MD simulated cell for HD12. The molecules are depicted by ball and stick model, and the hydrogen and oxygen atoms are shown in white and in red, respectively.
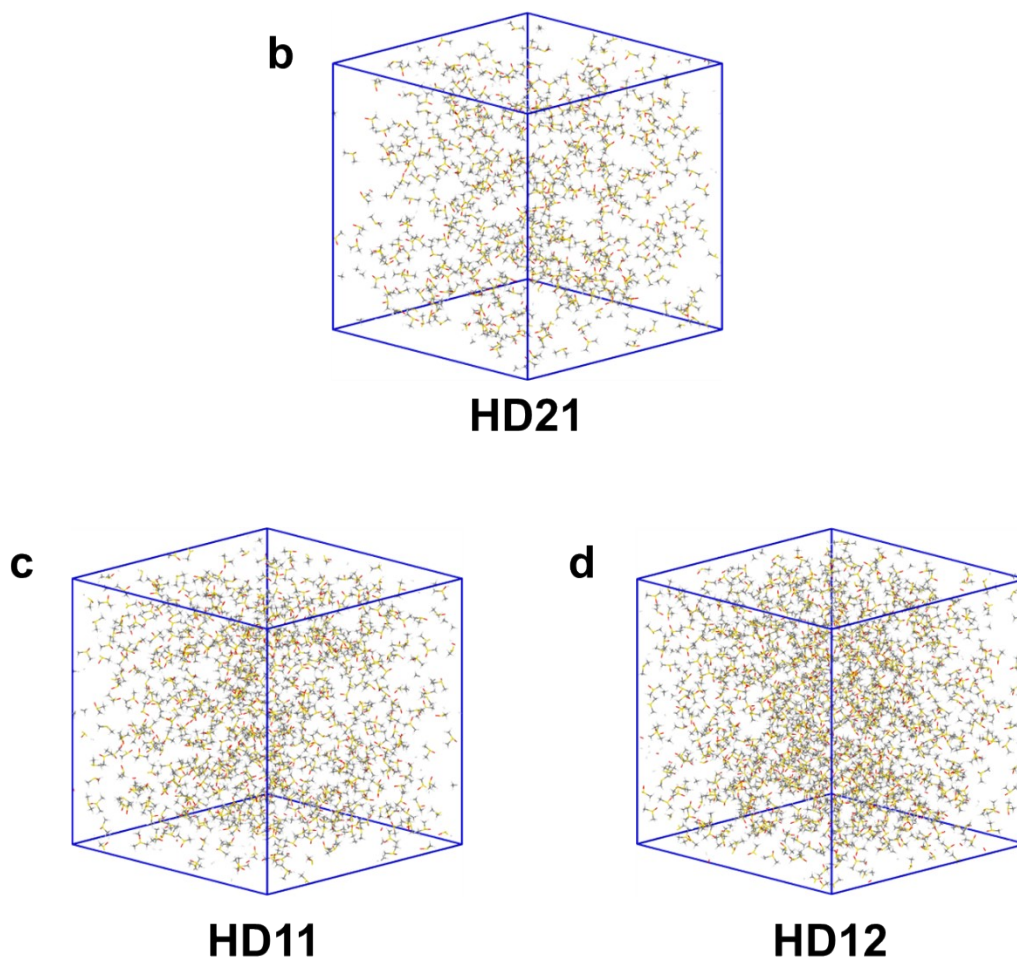
**Fig. S18 Continued.** Structure of hybrid electrolytes with different $H_2O$/DMSO volume ratios visualized by molecular dynamics (MD) simulation to highlight DMSO distribution. b) Snapshot of the MD simulated cell for HD21; c) Snapshot of the MD simulated cell for HD11; d) Snapshot of the MD simulated cell for HD12. The molecules are depicted by ball and stick model, and the carbon, hydrogen, oxygen and sulfur atoms are shown in gray, in white, in red and in yellow, respectively.

**Fig. S18 Continued.** Structure of hybrid electrolytes with different $H_2O$/DMSO volume ratios visualized by molecular dynamics (MD) simulation to highlight $Zn^{2+}$ distribution. a) Snapshot of the MD simulated cell for ZFE; b) Snapshot of the MD simulated cell for HD21; c) Snapshot of the MD simulated cell for HD11; d) Snapshot of the MD simulated cell for HD12. The molecules are depicted by ball and stick model, and the zinc atoms are shown in purple.

**Figure S19. RDF and CN**
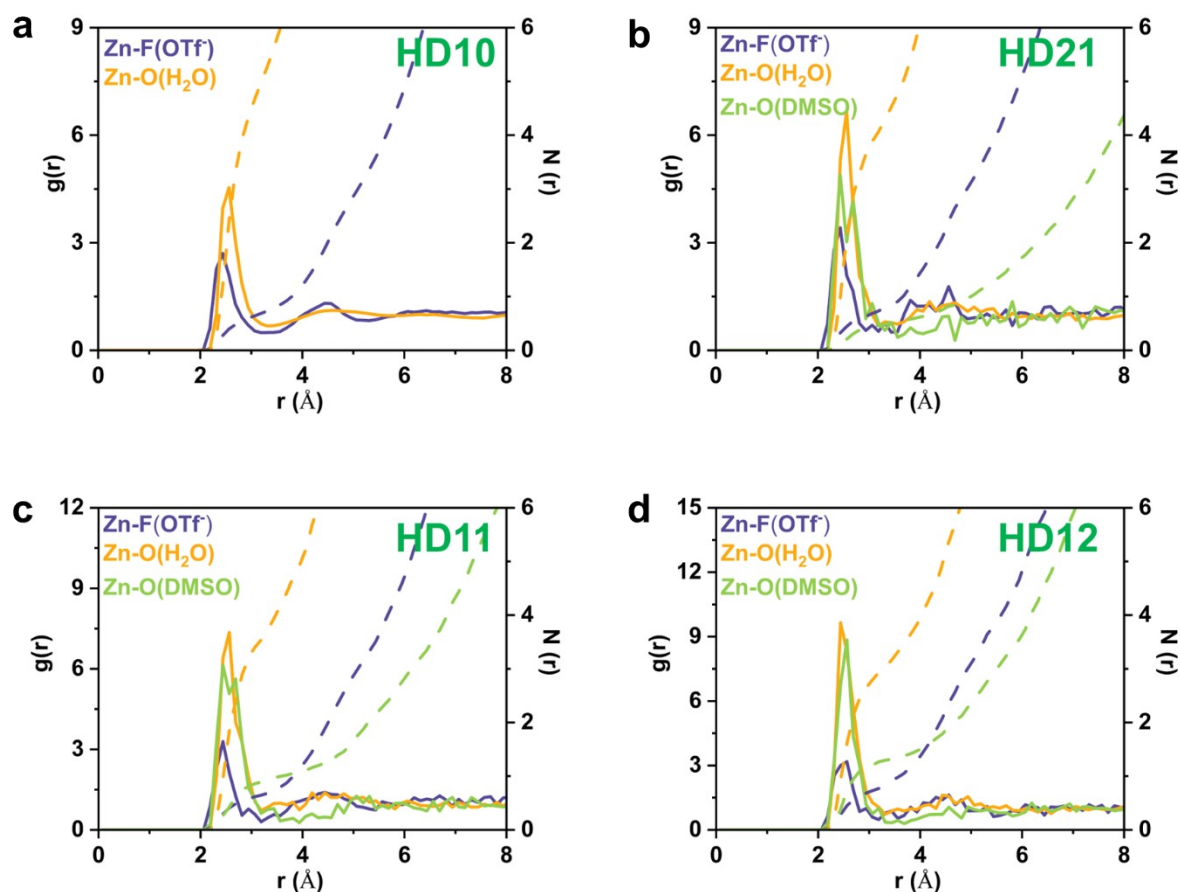


**Fig. S19** Radial distribution function (RDF) and coordination number (CN) for $Zn^{2+}$-$CF_3SO_3^-$ pairs, $Zn^{2+}$-$H_2O$ pairs and $Zn^{2+}$-DMSO pairs in ZFE and hybrid electrolytes. a) ZFE; b) HD21; c) HD11; d) HD12.

Molecular dynamics (MD) simulations are then conducted to compare the solvation structure between ZFE and hybrid electrolytes. The radial distribution function (RDF, g(r)) and corresponding coordination numbers (CN) are employed to probe the electrolyte structure in detail. The peaks of $Zn^{2+}$-$H_2O$ and $Zn^{2+}$-$CF_3SO_3^-$ both appear at around 2.3 Å, indicating the $Zn^{2+}$ is solvated by $H_2O$ and $CF_3SO_3^-$ in ZFE. In the hybrid electrolytes, the RDFs of $Zn^{2+}$-O (DMSO) exhibit a sharp peak around 2.3 Å, indicating DMSO participate in the $Zn^{2+}$ solvation sheath. In addition, CN of $Zn^{2+}$-$H_2O$ is 5.7 in ZFE, but it significantly decreases to 3.1 in HD12 electrolyte. While the N(r) of $Zn^{2+}$-O (DMSO) gradually increased from 0.7 to 1.6 as the increase of the content of DMSO. Meanwhile, CN of $Zn^{2+}$-$CF_3SO_3^-$ increases from 0.9 to 1.3. Therefore, hybrid electolytes possess the anion-involved and DMSO-rich solvation sheath.

.
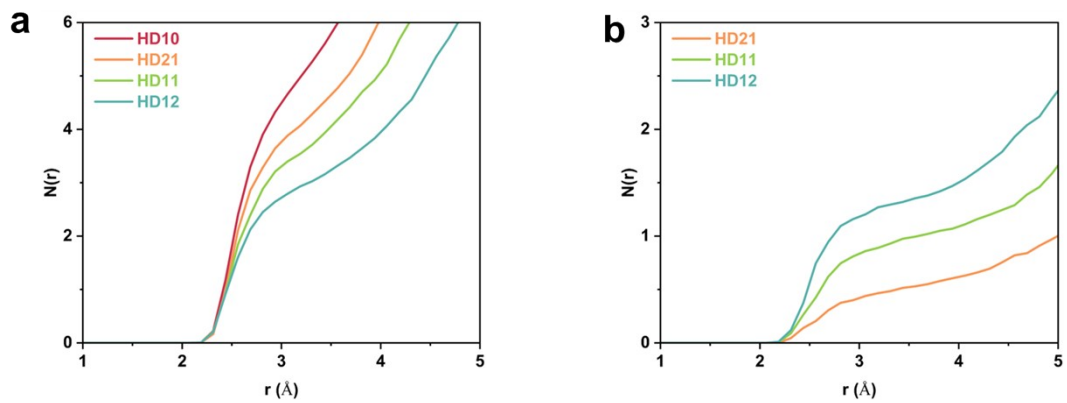
**Fig. S19 Continued.** Comparison of coordination number of H$_2$O and DMSO molecules in Zn$^{2+}$ solvation sheath of ZFE and hybrid electrolytes. a) The coordination number of H$_2$O; b) The coordination number of DMSO.

**Figure S20. Solvation struture ingredient analysis**
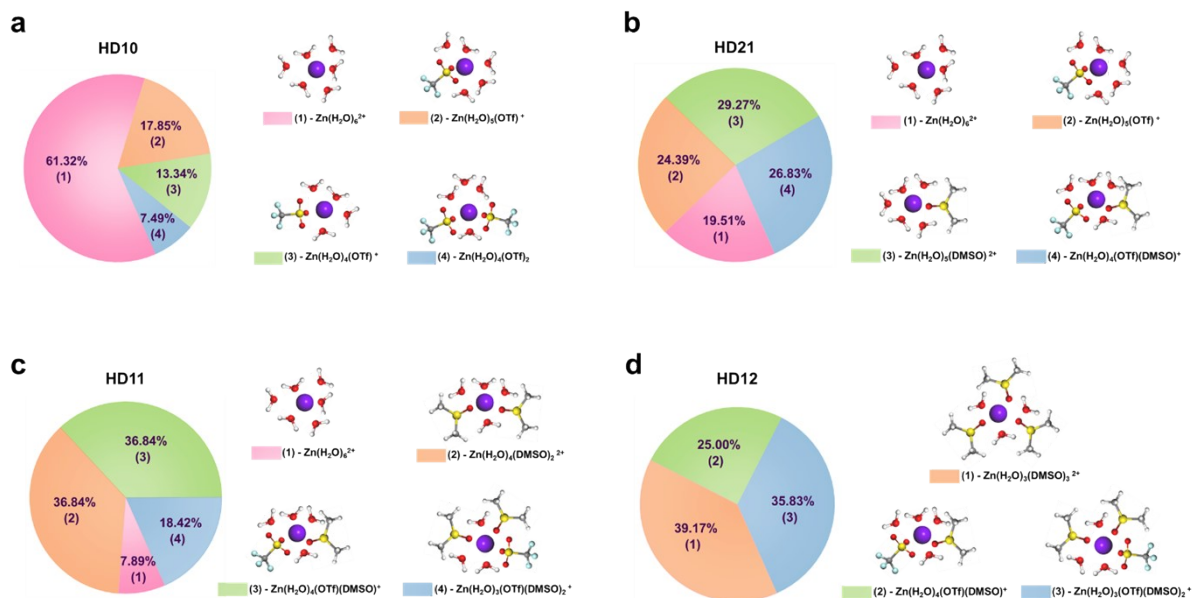


**Fig. S20** Distributions of the most probable compositions of $Zn^{2+}$ solvation sheaths with typical structures in different electrolytes from MD simulation. a) ZFE; b) HD21; c) HD11; d) HD12.

The most probable $Zn^{2+}$ solvation sheaths and their probabilities in each electrolyte are provided. In ZFE, the typical solvation structures of $Zn[H_2O]_6^{2+}$ is dominant and the proportion is as high as 61.32%. As the introduction of DMSO, the proportion of $Zn[H_2O]_6^{2+}$ is decreased sharply to 19.51%, 7.89%, and 0% for HD21, HD11 and HD12. For hybrid electrolytes, the primary solvation sheath of HD21, HD11 and HD12 electrolytes is $[Zn(H_2O)_5(DMSO)]^{2+}$, $[Zn(H_2O)_4(DMSO)]^{2+}$, and $[Zn(H_2O)_3(DMSO)_3]^{2+}$, which accounts for 29.27%, 36.84% and 39.17%, respectively. The secondary $Zn^{2+}$ solvation sheath is $[Zn(H_2O)_4(DMSO)(CF_3SO_3)^-]$, $[Zn(H_2O)_4(DMSO)(CF_3SO_3)^-]$ and $[Zn(H_2O)_3(DMSO)_2(CF_3SO_3)^-]$ for HD21, HD11 and HD12 electrolytes, whose proportion is 26.83%, 36.84%, and 35.83%, respectively. Moreover, with the increase of DMSO content in the electrolytes, the proportion of anion-involved solvation sheath increase from 29.63% in HD21 electrolyte to 70% in HD12 electrolyte. Therefore, the primary $Zn^{2+}$ solvation structure of hybrid electrolytes is DMSO-rich solvation sheath, and secondary $Zn^{2+}$ solvation structure is anion-involved solvation sheath.
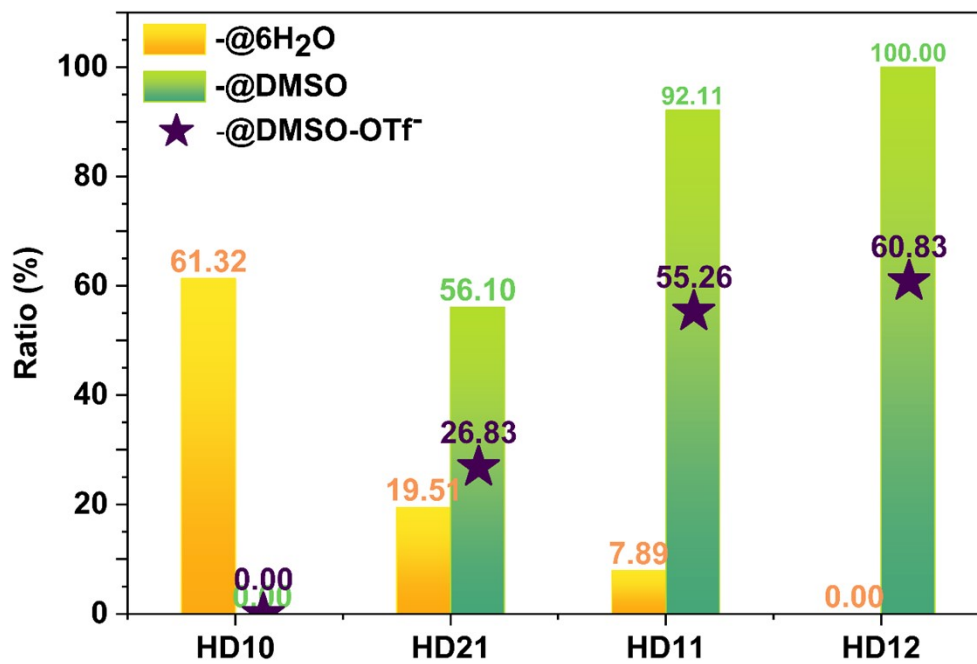
**Fig. S20 Continued.** Comparison of the proportions of two types of solvation shells in different electrolytes from MD simulation.

**Fig. S21** Representative $Zn^{2+}$ solvate species extracted from the MD simulations illustrating various compositions of $Zn^{2+}$ first solvation sheath for ZFE and hybrid electrolytes. a) ZFE; b) HD21; c) HD11; d) HD12.

**Figure S22. DFT calculation for free energy of $Zn^{2+}$ solvation struture**
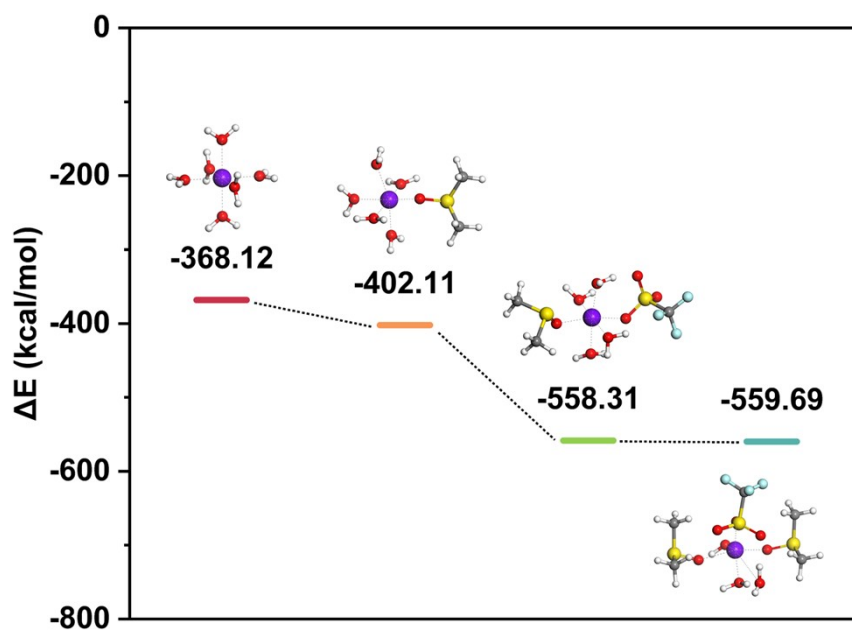


**Fig. S22** DFT calculation for free energy of $Zn^{2+}$ solvation structure. a) ZFE; b) HD21; c) HD11; d) HD12.

Compared with $Zn[H_2O]_6^{2+}$ in ZFE, the Gibbs free energy of $Zn(H_2O)_5(DMSO)^{2+}$, $Zn(H_2O)_4(OTf)(DMSO)^+$ and $Zn(H_2O)_3(OTf)(DMSO)_2^{2+}$ was significantly reduced to -402.11, 558.31, -559.69 kcal mol$^{-1}$, respectively.

**Figure S23. TOF-SIMS**
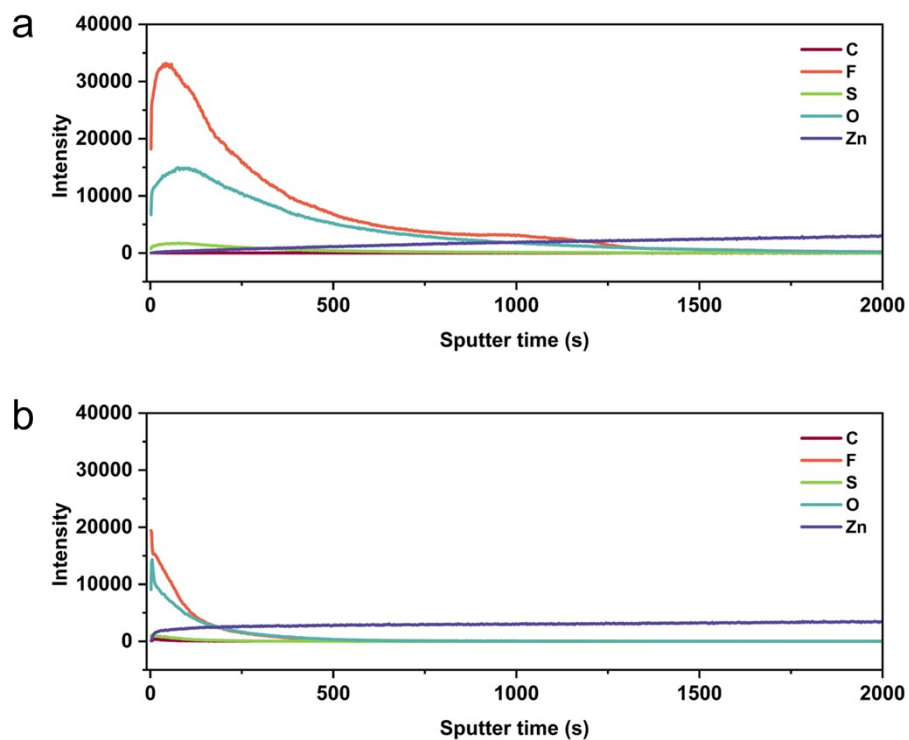


**Fig. S23** Time-of-flight secondary-ion mass spectrometry (TOF-SIMS) depth profiles of interesting element on the Zn anodes cycled in: a) ZFE and b) BPE.

Compared with ZFE, the element signals of Zn anode in BPE reach a faster balance during the sputtering time.
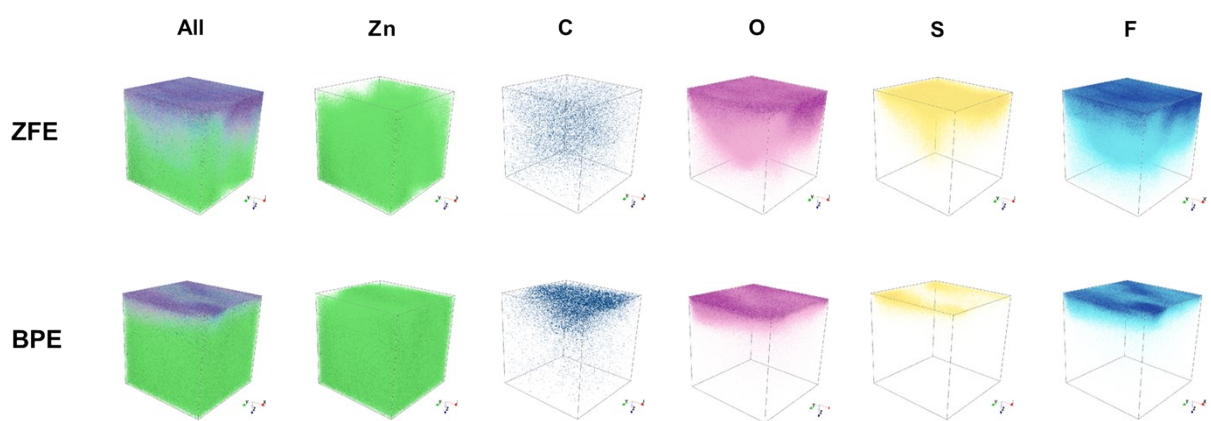
**Fig. S23 Continued.** Time-of-flight secondary-ion mass spectrometry (TOF-SIMS) characterization for Zn anode after 30 cycles in ZFE and BPE to highlight element spatial distribution.

**Figure S24. XPS survey spectra of SEI layer**



| Time | Atomic (%) | | | | |
|------|------|------|------|------|------|
| (min) | Zn | C | O | F | S |
| 0 | 25.56 | 24.84 | 39.94 | 6.01 | 3.65 |
| 2 | 54.9 | 3.15 | 34.66 | 4.84 | 2.45 |
| 10 | 71.21 | 2.06 | 24.76 | 1.14 | 0.83 |

| Time | Atomic (%) | | | | |
|------|------|------|------|------|------|
| (min) | Zn | C | O | F | S |
| 0 | 33.82 | 18.44 | 38.69 | 5.91 | 3.15 |
| 2 | 62.13 | 3.02 | 30.83 | 2.68 | 1.33 |
| 10 | 80.12 | 1.97 | 16.32 | 0.66 | 0.94 |
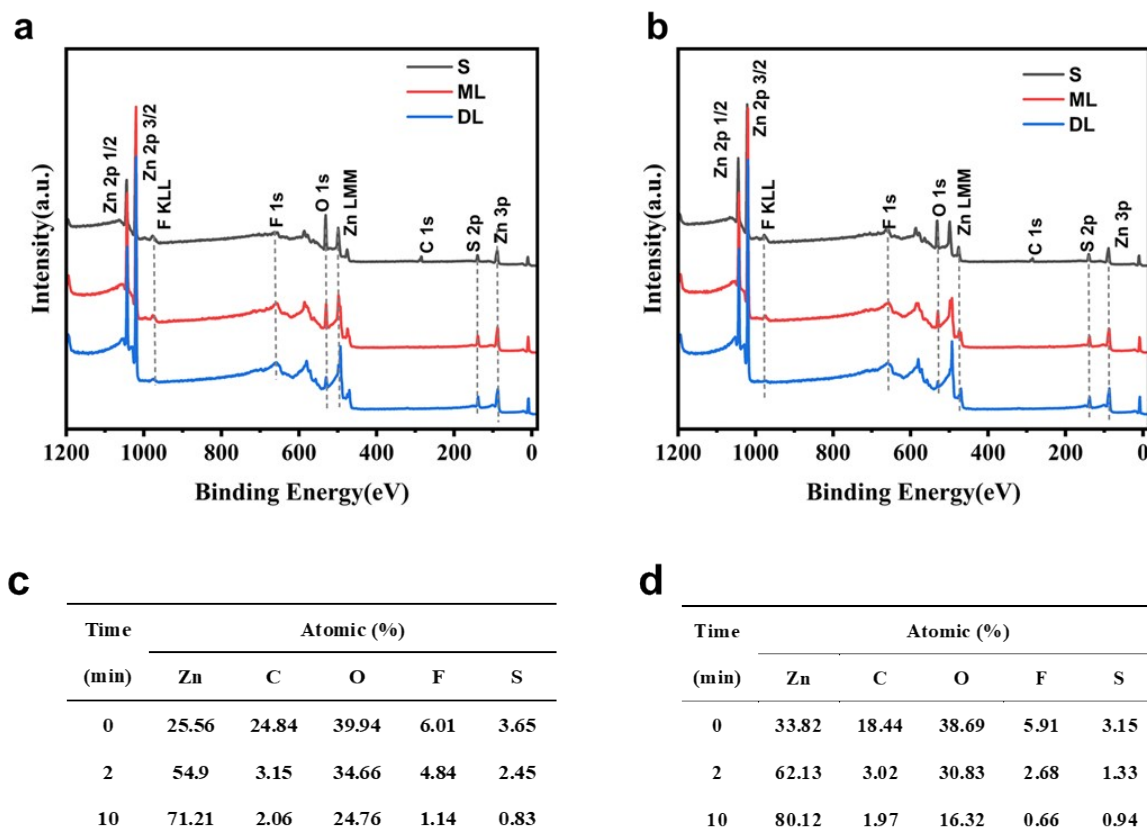
**Fig. S24** In-depth XPS survey spectra and elements content of Zn anode cycled in BPE after 30 cycles with different etching time (S: 0 min, ML: 2 min and DL:10 min). a, c) At room temperature; b, d) At low temperature.

X-ray photoelectron spectroscopy (XPS) coupled with Ar+ sputtering is conducted to detect the chemical composition of SEI of Zn anodes after 30 plating/stripping cycles at various sputtering time of 0 min, 2 min and 10 min in BPE. The corresponding quantitative content of different elements are presented in **Fig. S24**, and all binding energies are calibrated by using the C 1s peak (at 284.8 eV) as the reference.

Unfortunately, owning to the complexity of SEI composition and formation mechanism, quantifying the content of different components for SEI formation is still a daunting challenge for battery community. Although the SEI of lithium batteries has been investigated for decades, the structure and chemical composition of SEI are still not fully understood due to the difficulty to getting direct experimental evidence. The development of advanced in-situ characterization technologies for quantifying the content of each component will be well worth exploring by the community of aqueous zinc ion batteries.

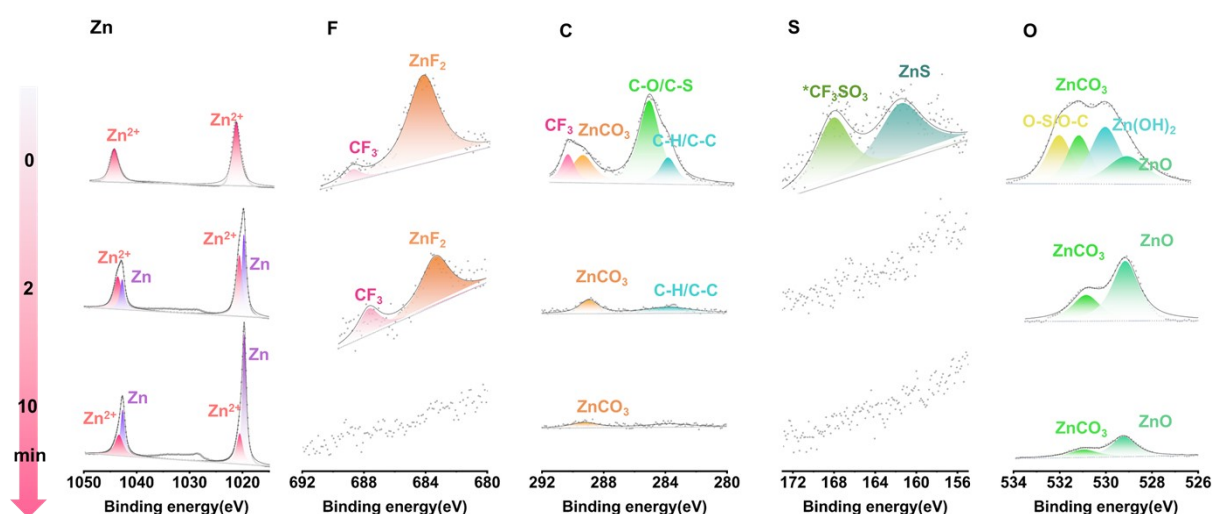**Figure S25. In-depth XPS spectra of SEI layer at room temperature**
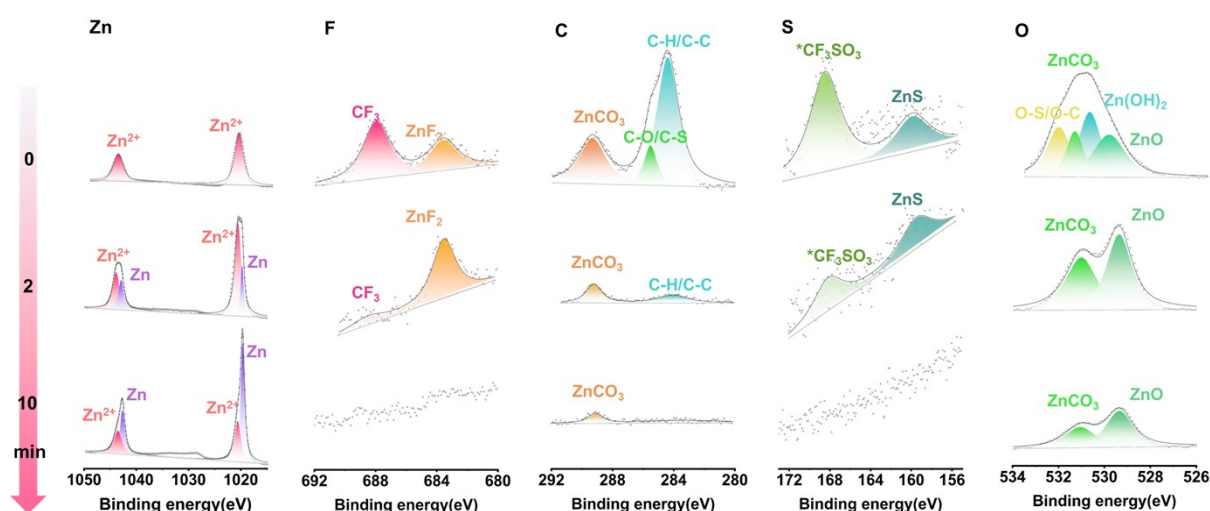


**Fig. S25** XPS spectra with in-depth profiles of Zn anode after 30 cycles in BPE at room temperature (25°C) with different etching time (0 min, 2 min and 10 min). a) $Zn_{2p}$ XPS spectra with in-depth profiles; b) F1s XPS spectra with in-depth profiles; c) $C_{1s}$ XPS spectra with in-depth profiles; d) $O_{1S}$ XPS spectra with in-depth profiles; e) $S_{1S}$ XPS spectra with in-depth profiles.

In the Zn 2p spectra from XPS, both Zn and $Zn^{2+}$ signals can be clearly distinguished. with the increase of $Ar^+$ etching time, the total percentage of Zn element increases from 25.6% on the topmost surface to 54.9% at 5 min and 71.2% at 10 min, and meanwhile the $Zn^{2+}$ content decreases while Zn metal content increases.

In the F1s spectra, both organic fluorine ($CF_3$) at 688.4 eV and inorganic fluorine ($ZnF_2$, at 684.6 eV) can be observed on Zn anode, and organic fluorine is mainly distributed on the surface of SEI layer, which indicates the $CF_3SO_3^-$ anions also participate in the formation of the SEI layer via electrochemical decomposition. With the increase of $Ar^+$ etching time to 2 min, $ZnF_2$ can be still detected, and the $ZnF_2$ content significantly increases compared with that on surface, suggest the organic-rich upper layer and inorganic-rich sublayer of SEI.

In the C1s XPS spectra, the peaks at 289.7, 285.8 and 284.8 eV are attributed to $ZnCO_3$, C-O/C-S and C-H/C-C, respectively, and C-H/C-C component possesses much highest content. As $Ar^+$ sputtering consistently proceeds, inorganic $ZnCO_3$ still presents, while the organic C-O/C-S and C-H/C-C are missing, indicating that organic carbon species enriches in the upper-layer of SEI and inorganic carbon species is abundant in the sub-layer of SEI. The C-H/C-C component arises from the decomposition of DMSO or $CF_3SO_3^-$ anion; C-O/C-S component is mainly derived from DMSO decomposition; and $ZnCO_3$ results from either $CF_3SO_3^-$ anion decomposition or dissolved $CO_2$ in electrolytes.

For the O1s spectra, organic O-S/O-C (532.4 eV) and $ZnCO_3$ (531.2 eV) are clearly observed on the SEI surface, which further confirmed the decomposition of DMSO and $CF_3SO_3^-$ anion, as recognized by C1s spectra. As the $Ar^+$ sputtering time increases, organic O-S/O-C component quickly disappears, while inorganic components can be still detected at the etching time of 5 min and 10 min.

S2p XPS spectra confirms the existence of $*CF_3SO_3$ component (168.3 eV) and ZnS (at 162.1 eV), which verifies the decomposition of $CF_3SO_3^-$ anions, being in accordance with the F1s spectra. ZnS disappears but $*CF_3SO_3$ is still detected at the etching time of 2min.

**Figure S26. In-depth XPS spectra of SEI layer at low temperature of -20 ℃**



**Fig. S26** XPS spectra with in-depth profiles of Zn anode after 30 cycles in BPE at low temperature (-20 ℃) with different etching time (0 min, 2 min and 10 min). a) $Zn_{2p}$ XPS spectra with in-depth profiles; b) F1s XPS spectra with in-depth profiles; c) $C_{1s}$ XPS spectra with in-depth profiles; d) $O_{1S}$ XPS spectra with in-depth profiles; e) $S_{1S}$ XPS spectra with in-depth profiles.

The low-temperature SEI exhibit similar chemical components with room-temperature SEI except a few alterations of the content and distribution of certain components. In the Zn2p XPS spectra of low-temperature SEI, Zn metal content is much higher than that of room-temperature SEI at the same etching time, which suggests the thinner SEI layer at low-temperature, being similar with the thinner low-temperature SEI of lithium metal batteries. Similarly, F1S XPS spectra confirms the existence of inorganic $ZnF_2$ and organic $*CF_3SO_3$ in low-temperature SEI layer, both upper layer and sublayer of SEI contains higher $ZnF_2$ component. Low-temperature SEI shows the similar carbon components, but the C-O/C-S species becomes the dominated component, which is attributed to different effects of temperature on interfacial reaction kinetics. The faster disappearance of carbon components further confirms the thinner SEI. O1s XPS spectra further indicate the SEI layer at low-temperature comprising organic-rich upper layer and inorganic-rich sublayer. In the S1s XPS spectra, ZnS and $*CF_3SO_3$ is mainly distributed on the SEI surface at low temperature. The favorable low-temperature SEI layer effectively impedes the water penetration, reduces side reactions and guide $Zn^{2+}$ deposition, which prolongs the lifespan of Zn anodes.

**Figure S27. Zn||Zn symmetric cell with ZFE**
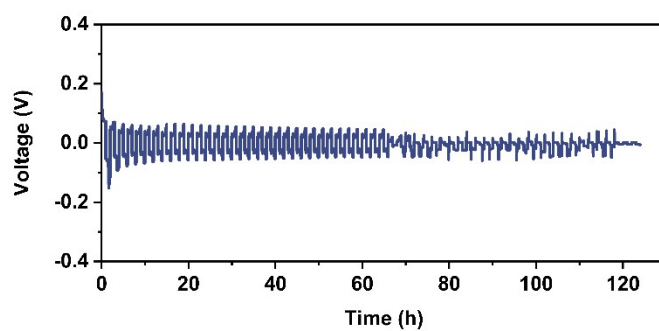


**Fig. S27** Cycling performance of Zn||Zn symmetric cell with ZFE at $0.5\,\mathrm{mA\cdot cm^{-2}}$ and $0.5\,\mathrm{mAh\cdot cm^{-2}}$.

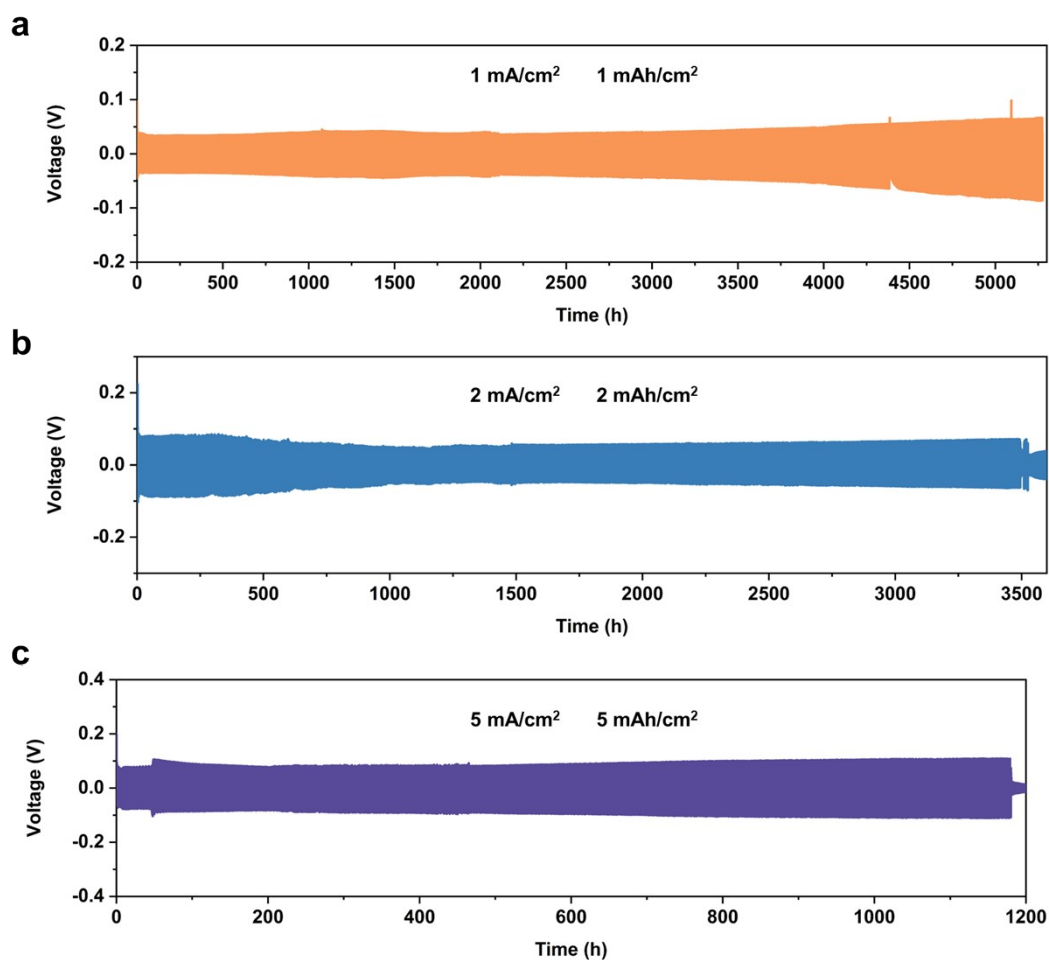**Figure S28. Zn||Zn symmetric cell with different electrolytes**
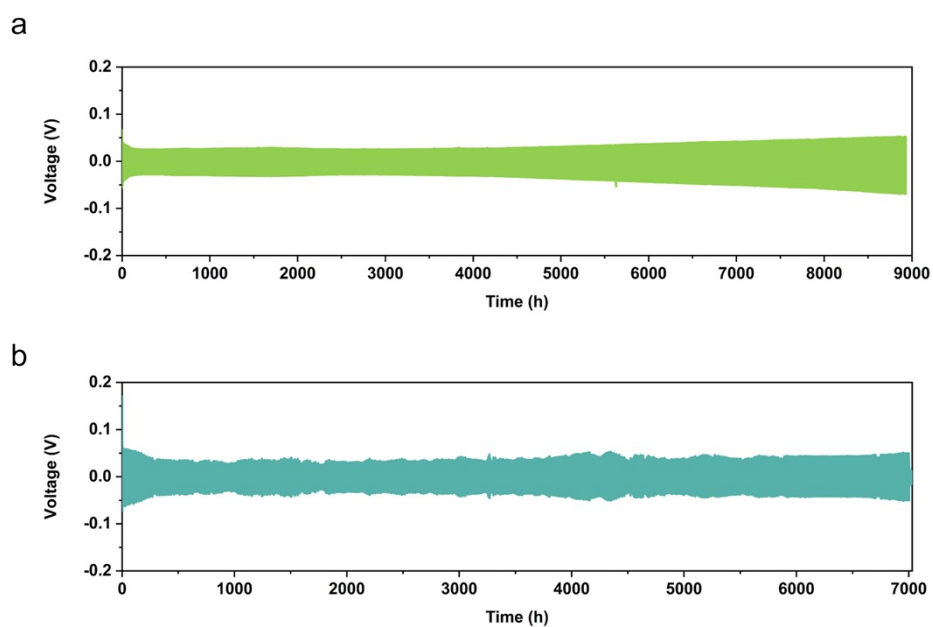


**Fig. S28** Cycling performance of Zn||Zn symmetric cell with different electrolytes. a) Galvanostatic Zn stripping/plating in the Zn||Zn symmetric cell with HD21 electrolyte at 0.5 mA·cm$^{-2}$ and 0.5 mAh·cm$^{-2}$; b) Galvanostatic Zn stripping/plating in the Zn||Zn symmetric cell with HD12 electrolyte at 0.5 mA·cm$^{-2}$ and 0.5 mAh·cm$^{-2}$.

**Figure S29. Rate performance of Zn||Zn symmetric cell with ZEF at different current densities.**
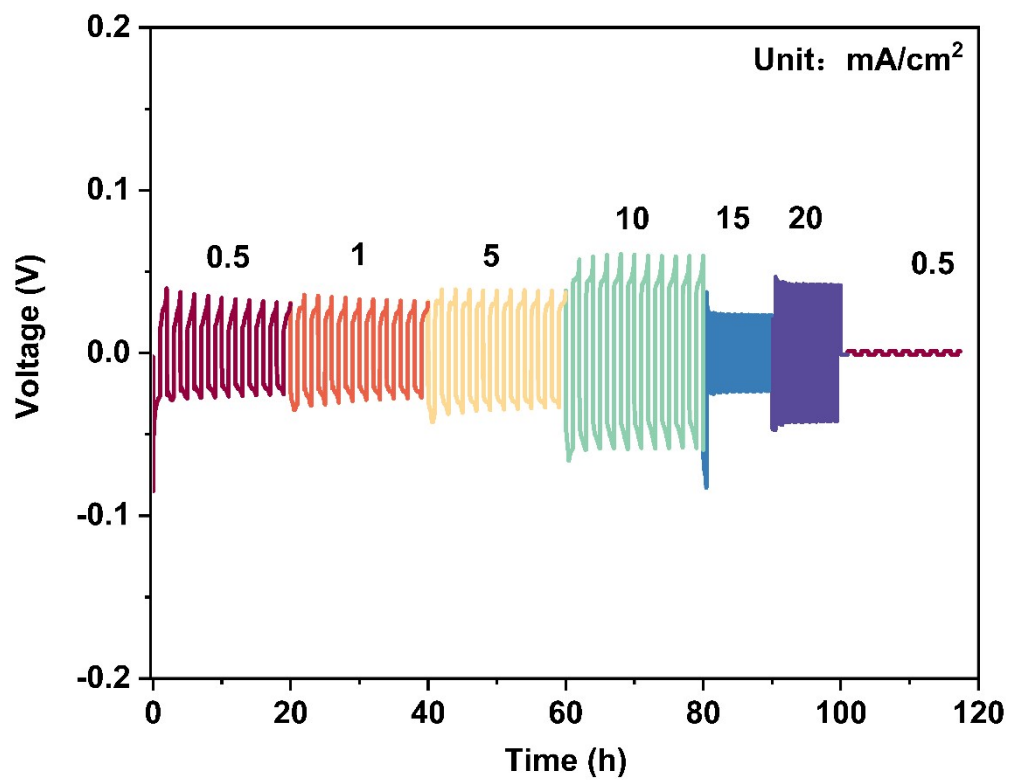


**Fig. S29** Rate performance of Zn||Zn symmetric cell with ZEF at different current densities.

**Figure S30. Zn||Zn symmetric cell at different current densities**



**Fig. S30** Cycling performance of Zn||Zn symmetric cell at different current densities. a) Galvanostatic Zn stripping/plating in the Zn||Zn symmetric cell with BPE at 1 mA·cm$^{-2}$ and 1 mAh·cm$^{-2}$; b) Galvanostatic Zn stripping/plating in the Zn||Zn symmetric cell with BPE at 2 mA·cm$^{-2}$ and 2 mAh·cm$^{-2}$; c) Galvanostatic Zn stripping/plating in the Zn||Zn symmetric cell with BPE at 5 mA·cm$^{-2}$ and 5 mAh·cm$^{-2}$.

**Figure S31. Zn||Ti asymmetric cell with ZFE and BPE**
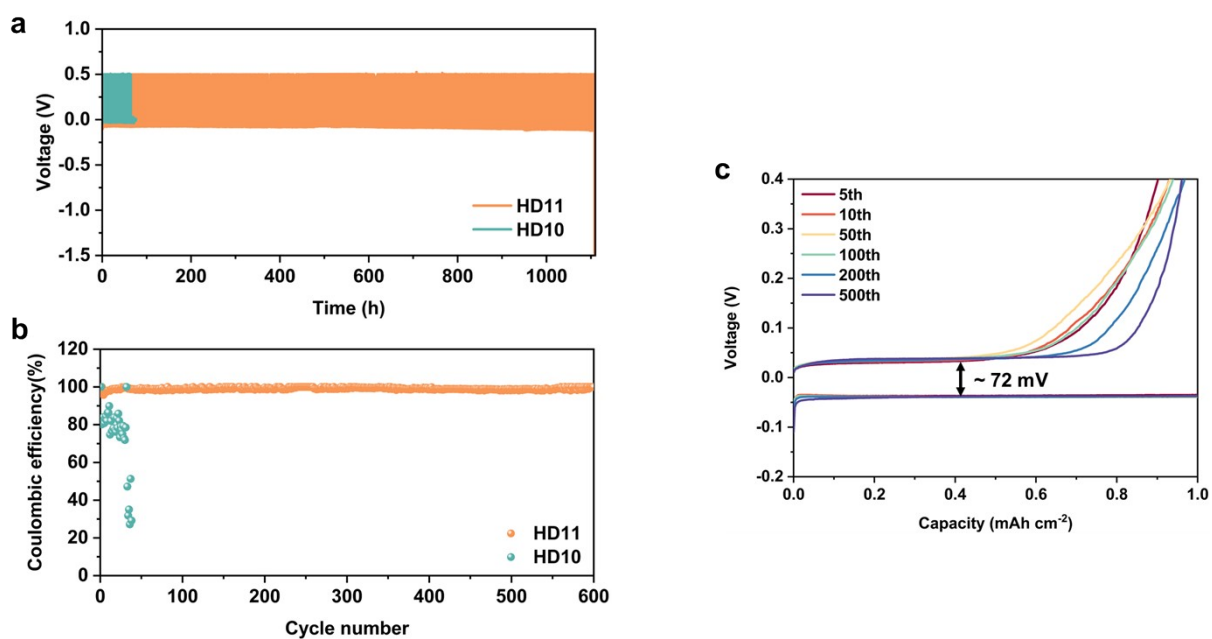


**Fig. S31** Electrochemical performance of Zn||Ti asymmetric cell. a) Galvanostatic Zn plating/stripping in the Zn||Ti asymmetric cell with ZFE and BPE at $1\,mA\cdot cm^{-2}$ and $1\,mAh\cdot cm^{-2}$; b) Coulombic efficiency (CE) of Zn||Ti asymmetric cell with ZFE and BPE at $1\,mA\cdot cm^{-2}$ and $1mAh\cdot cm^{-2}$; c) Zn stripping/plating voltage curves of BPE.

**Figure S32. Zn||Cu asymmetric cell with BPE**
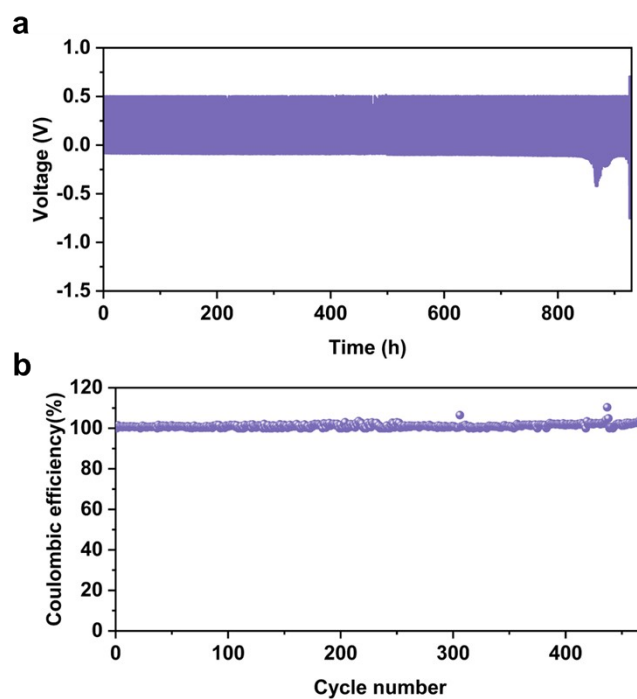


**Fig. S32** Electrochemical performance of Zn||Cu asymmetric cell with BPE. a) Galvanostatic Zn plating/stripping in the Zn||Cu asymmetric cell with BPE at 1 mA·cm$^{-2}$ and 1 mAh·cm$^{-2}$; b) Coulombic efficiency (CE) of the Zn||Cu asymmetric cell with BPE at 1 mA·cm$^{-2}$ and 1 mAh·cm$^{-2}$.

**Figure S33. Zn||Zn symmetric cell at low temperature**
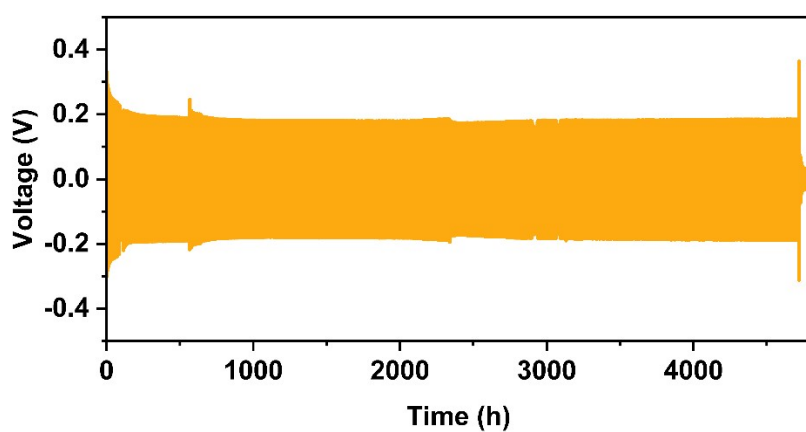


**Fig. S33** Cycling performance of Zn||Zn asymmetric at low temperature. Galvanostatic Zn stripping/plating in the Zn||Zn symmetric cell with BPE at $0.5\,mA\cdot cm^{-2}$ and $0.5\,mAh\cdot cm^{-2}$ under -20 ℃.

**Figure S34. SEM images of Zn anodes cycled in different electrolytes**
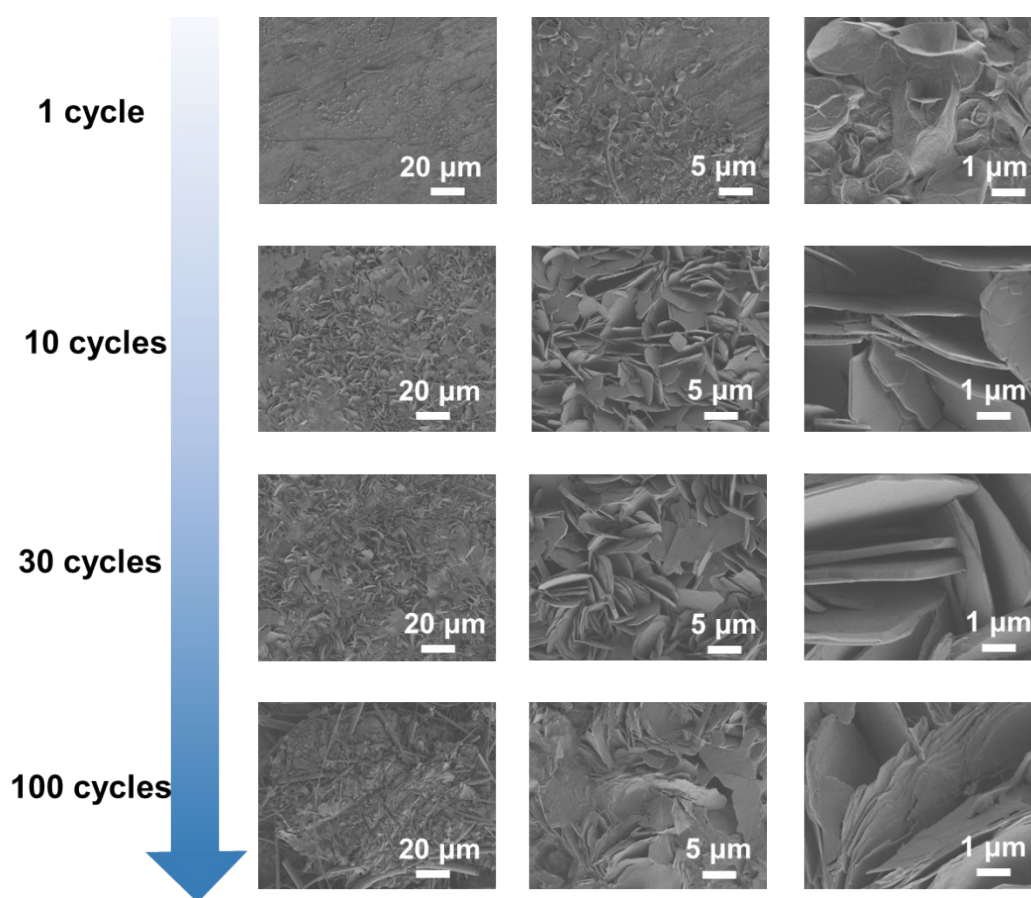


**Fig. S34** Scanning electron microscopy (SEM) images of zinc anode in Zn//Zn symmetric cells with ZFE after 30 cycles under a test condition of 0.5 mA·cm$^{-2}$ and 0.5 mAh·cm$^{-2}$ at room temperature.
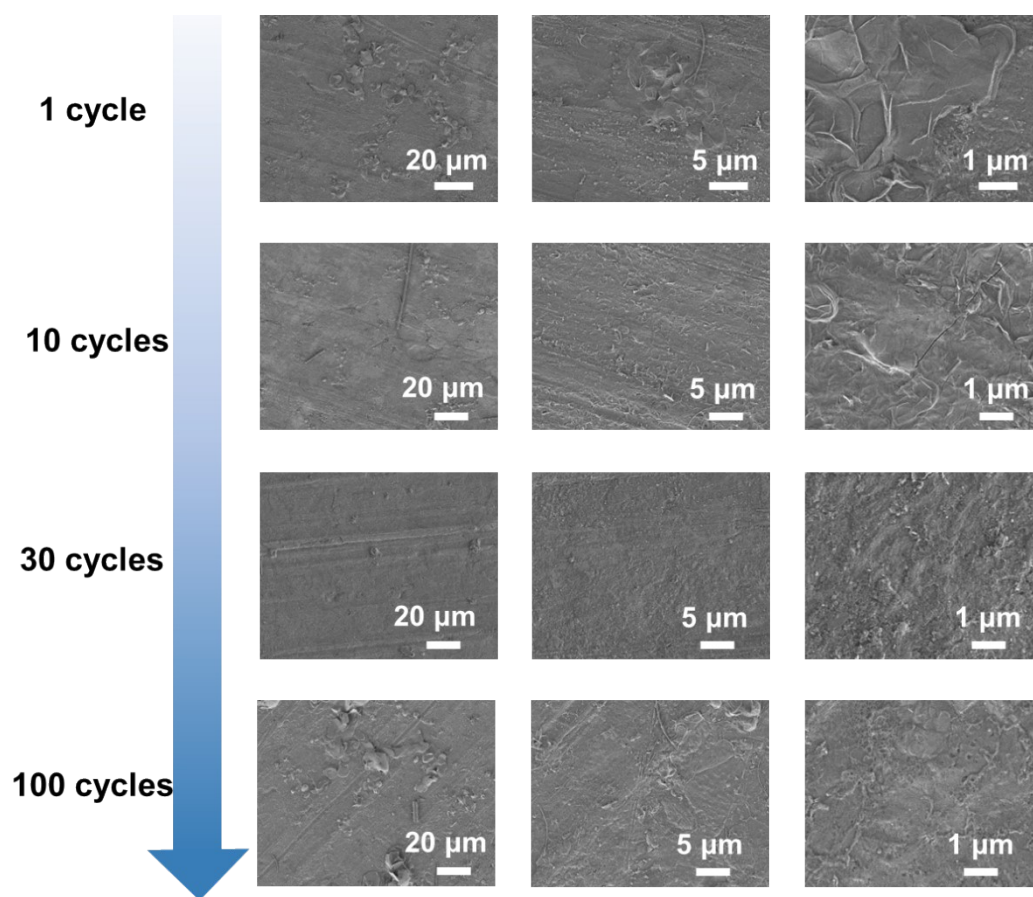
**Fig. S34 Continued.** Scanning electron microscopy (SEM) images of zinc anode in Zn//Zn symmetric cells with HD21 hybrid electrolyte after 30 cycles under a test condition of 0.5 mA·cm$^{-2}$ and 0.5 mAh·cm$^{-2}$ at room temperature.
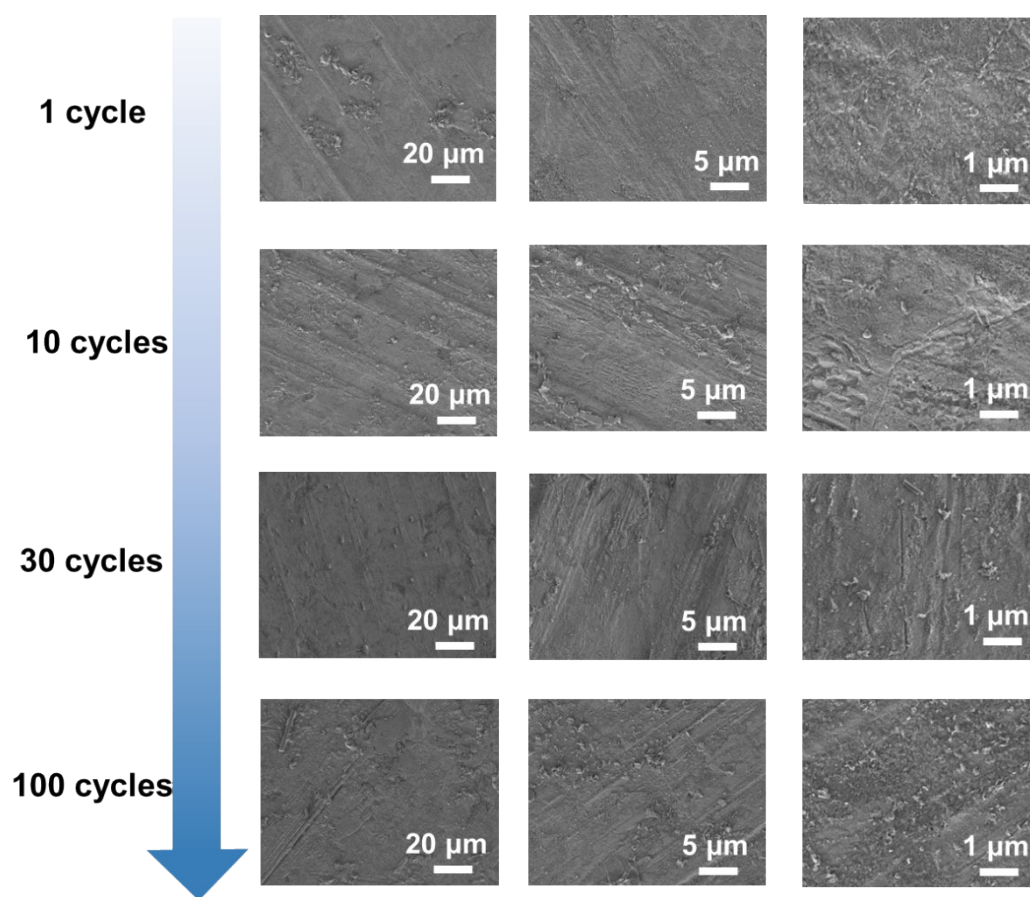
**Fig. S34 Continued.** Scanning electron microscopy (SEM) images of zinc anode in Zn//Zn symmetric cells with HD11 hybrid electrolyte after 30 cycles under a test condition of 0.5 mA·cm$^{-2}$ and 0.5 mAh·cm$^{-2}$ at room temperature.
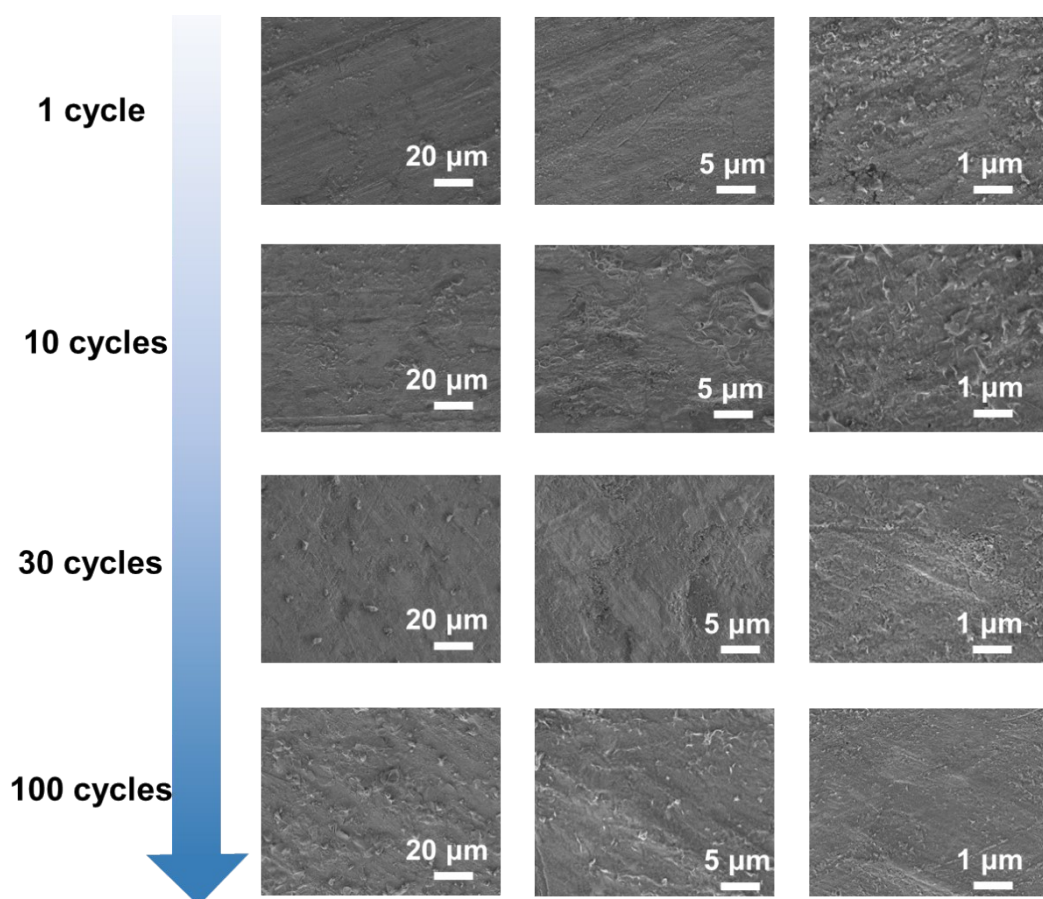
**Fig. S34 Continued.** Scanning electron microscopy (SEM) images of zinc anode in Zn//Zn symmetric cells with HD12 hybrid electrolyte after 30 cycles under a test condition of 0.5 mA·cm$^{-2}$ and 0.5 mAh·cm$^{-2}$ at room temperature.

**Figure S35. FIB-SEM images of Zn anodes**
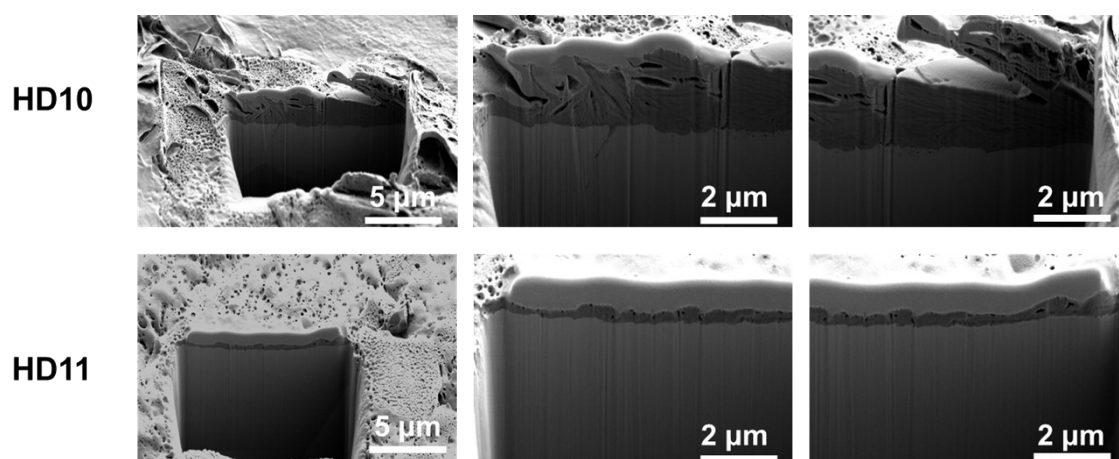


**Fig. S35** Focused Ion Beam Scanning Electron Microscopy (FIB-SEM) characterization for the three-dimensional morphology of Zn anodes in Zn//Zn symmetric cells with ZFE (a) and BPE (b) after 30 cycles under a test condition of 0.5 mA·cm$^{-2}$ and 0.5 mAh·cm$^{-2}$ at room temperature (25 ℃).

**Figure S36. SEM images of Zn anodes with different cycling times**

## 1 mA/cm² 1200 hours
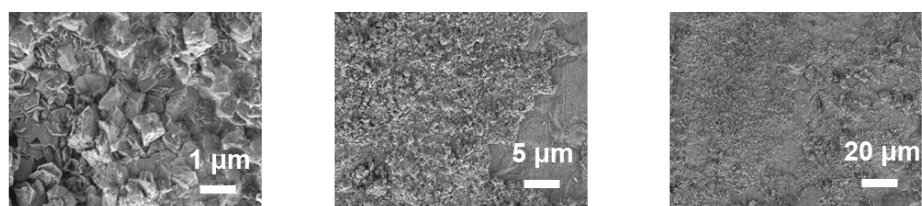


## 1 mA/cm² 4500 hours
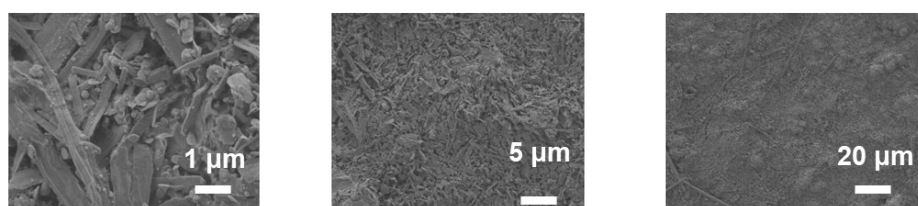


## 2 mA/cm² 3200 hours
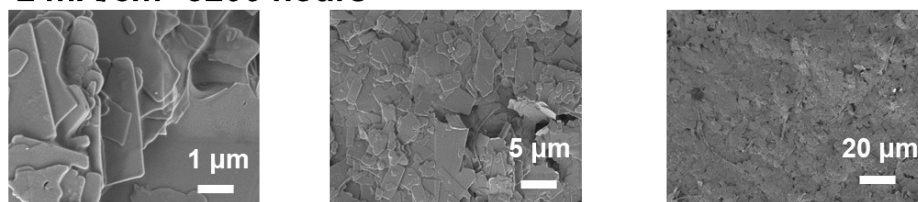


## 5 mA/cm² 1200 hours
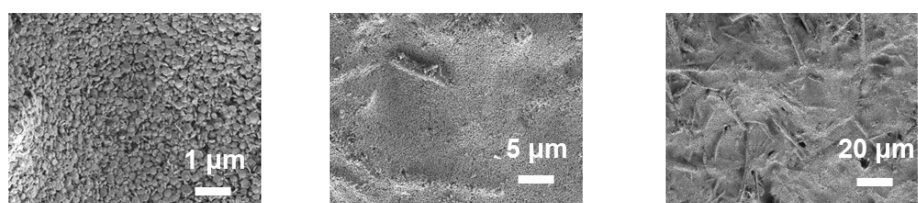


**Fig. S36** Scanning electron microscopy (SEM) characterization of zinc anodes in BPE after long-term cycling time at different current densities.

**Figure S37. SEM images of Zn anodes at low temperatures**
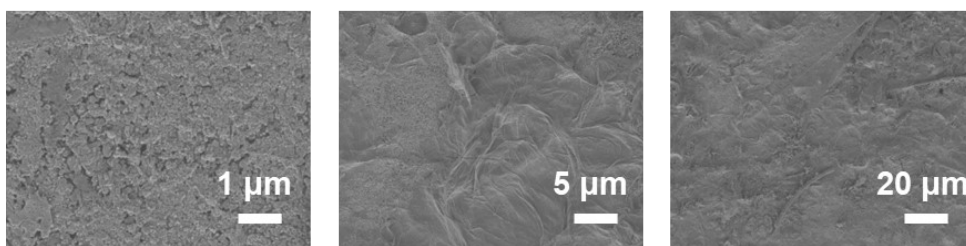
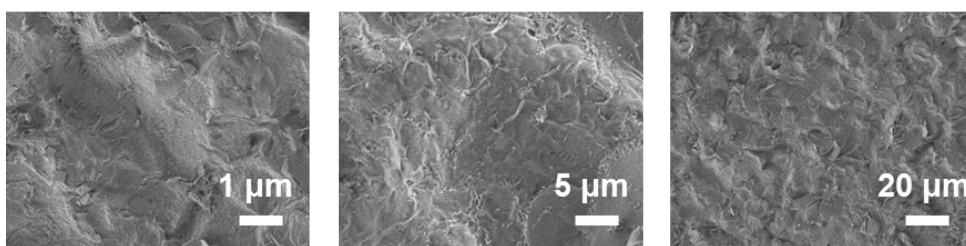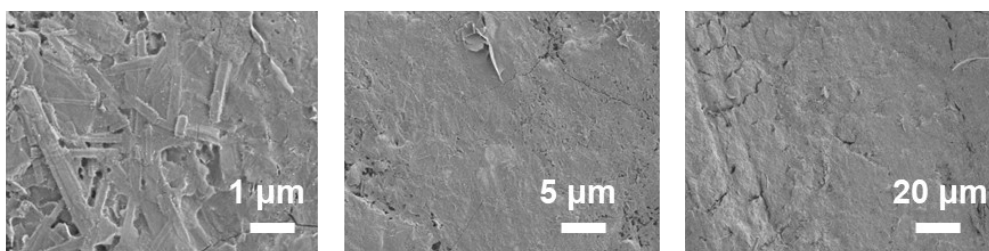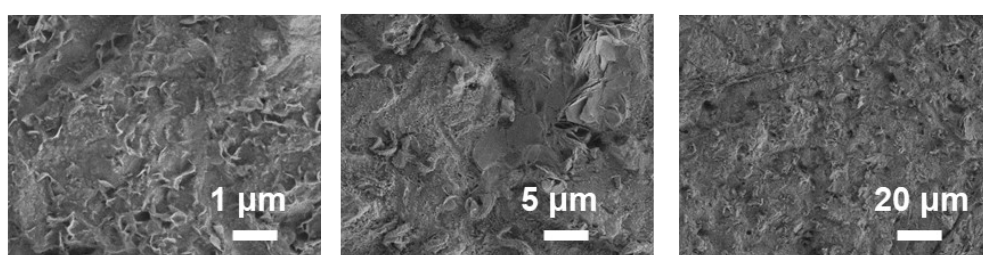## -20 ℃ 0.5 mA/cm² 30 cycle



## -60 ℃ 0.2 mA/cm² 30 cycle



**Fig. S37** Scanning electron microscopy (SEM) characterization of zinc anode after 30 cycles in Zn//Zn symmetric cells with BPE under different low temperatures of -20 ℃ and -60 ℃.

**Figure S38. SEM images of Zn anodes after long cycling at low temperatures**

## -20 ℃ 1000 hours


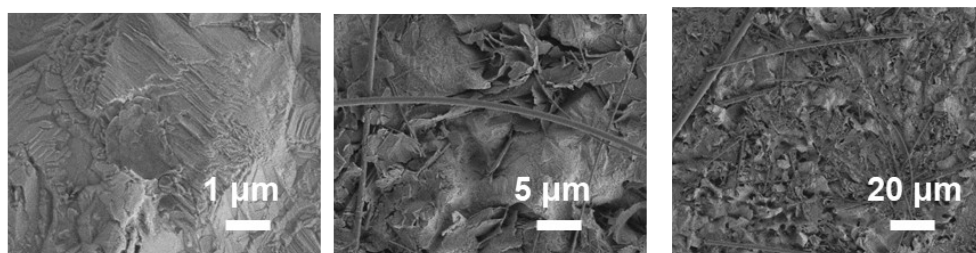
## -20 ℃ 2000 hours



## -20 ℃ 4000 hours



**Fig. S38** Scanning electron microscopy (SEM) characterization of zinc anode evolution after different cycles in Zn//Zn symmetric cells with BPE under a test condition of 0.5 mA·cm$^{-2}$ and 0.5 mAh·cm$^{-2}$ at -20 °C. a) Surface SEM images of Zn anode after 1000 hours; b) Surface SEM images of Zn anode after 2000 hours; c) Surface SEM images of Zn anode after 4000 hours.

The deposited Zn metal is smooth and compact in HD11 electrolyte at -20 °C after cycling for 1000 hours. As Zn plating/stripping goes to 2000 hours, some protrusions are detected on the Zn anode surface. After 4000 hours, the protrusions grow up and some small-sized Zn plates perpendicular to the Zn anode can also be observed, which further indicates the BPE can effectively relieve Zn dendrite growth and significantly prolong the cycling stability of Zn anode.

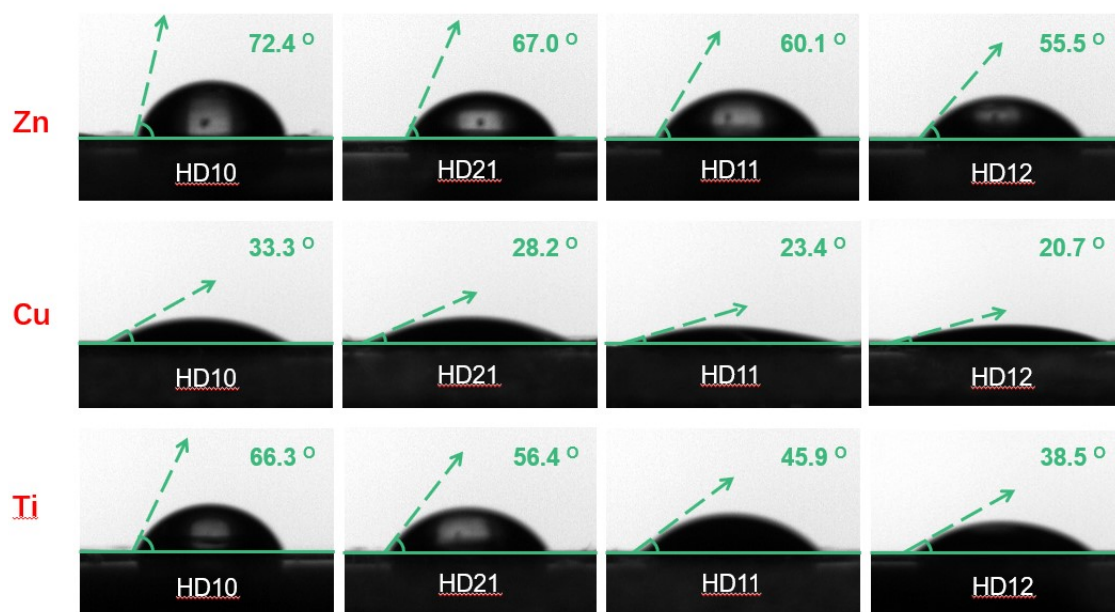**Figure S39. Electrolyte-electrode contact angles**



**Fig. S39** Contact angles of ZFE and hybrid electrolytes to Zn, Cu and Ti electrodes.
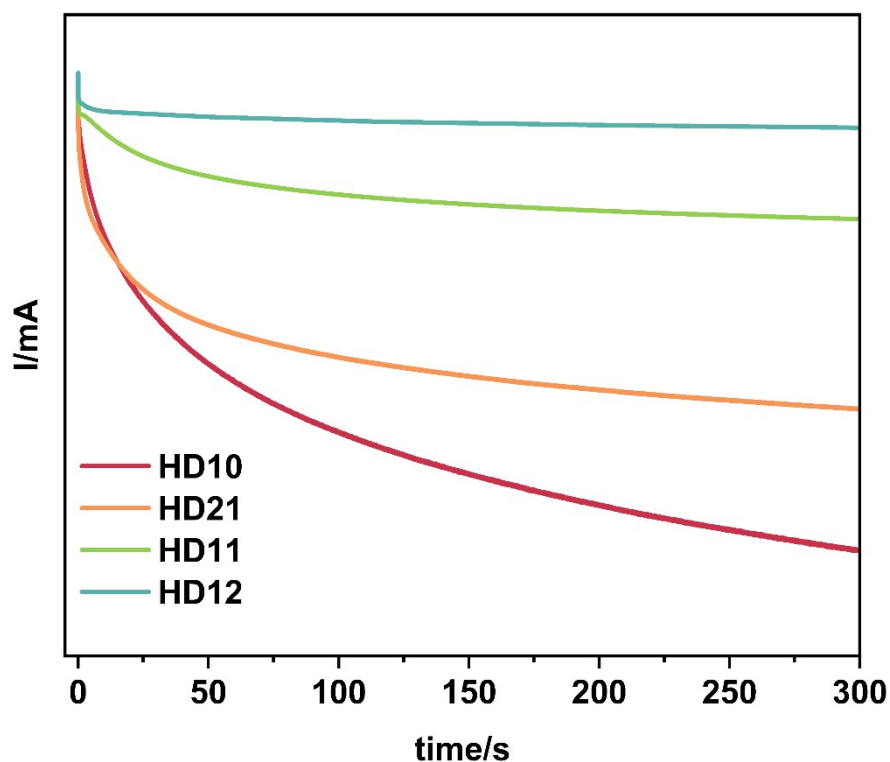
**Figure S40. CA curves**



**Fig. S40** Chronoamperometric curves of Zn electrodeposition in ZFE and hybrid electrolytes under -150 mV.

    Chronoamperometry (CA) is conducted under a constant overpotential of -150 mV to characterize the $Zn^{2+}$ diffusion on Zn anode. In the ZFE, the current response is continuously increasing, indicating a continuous $Zn^{2+}$ 2D diffusion process, which may be caused by the increase of the effective electrode area due to dendrite growth. Conversely, for zinc anode cycled in the hybrid electrolytes, the current response shows the inappreciable change beyond the initial 100 s, suggesting the hindered 2D surface diffusion. Therefore, it is deduced that dendrite growth is well suppressed and the dense and smooth deposition layer can be easily achieved.
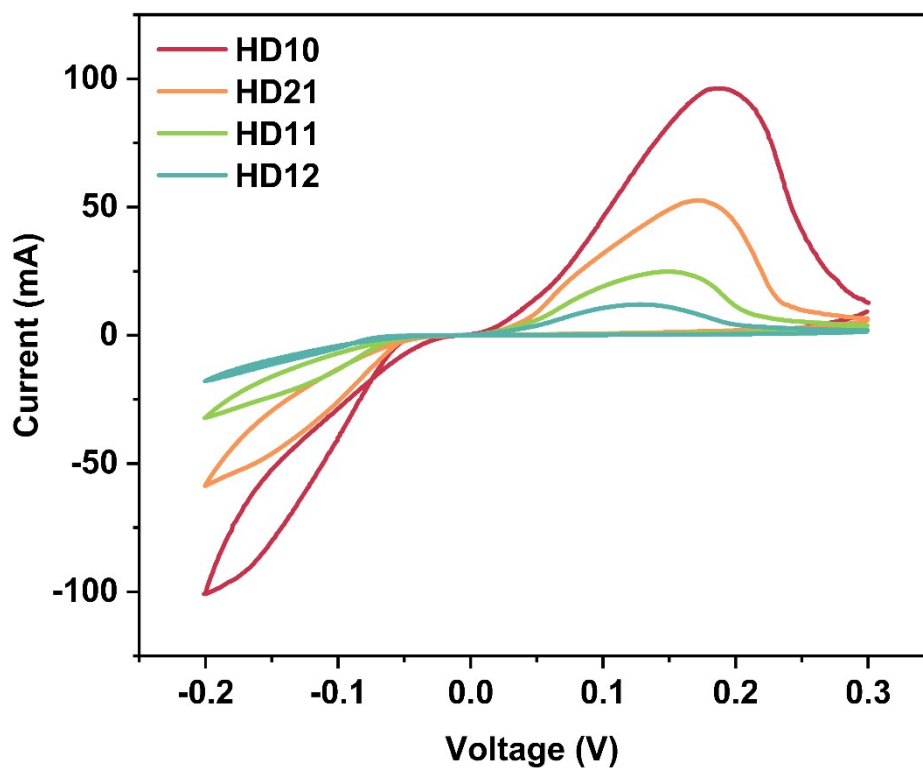
**Figure S41. CV curves**



**Fig. S41** Cyclic voltammograms for Zn nucleation on zinc anode in ZFE and hybrid electrolytes

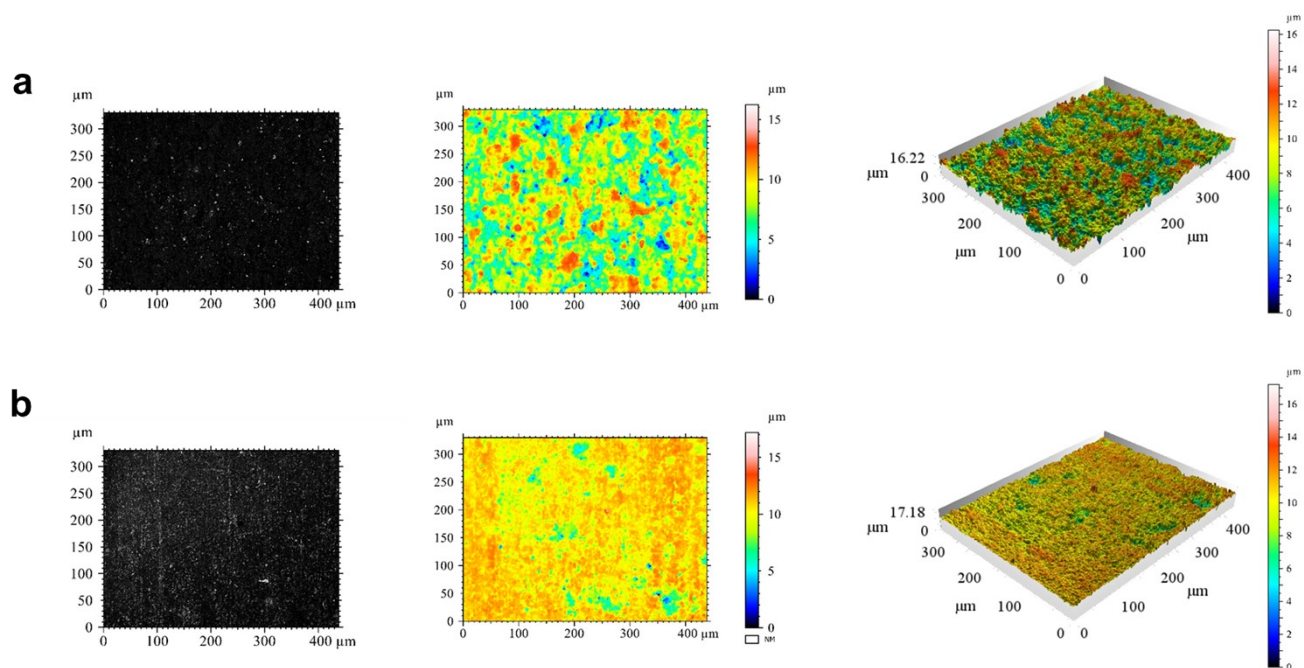**Figure S42. Laser confocal scanning microscope (LCSM)  characterization**



**Fig. S42** Laser confocal scanning microscope (LCSM) chracterization for Zn plating in: a) ZFE and b) BPE.
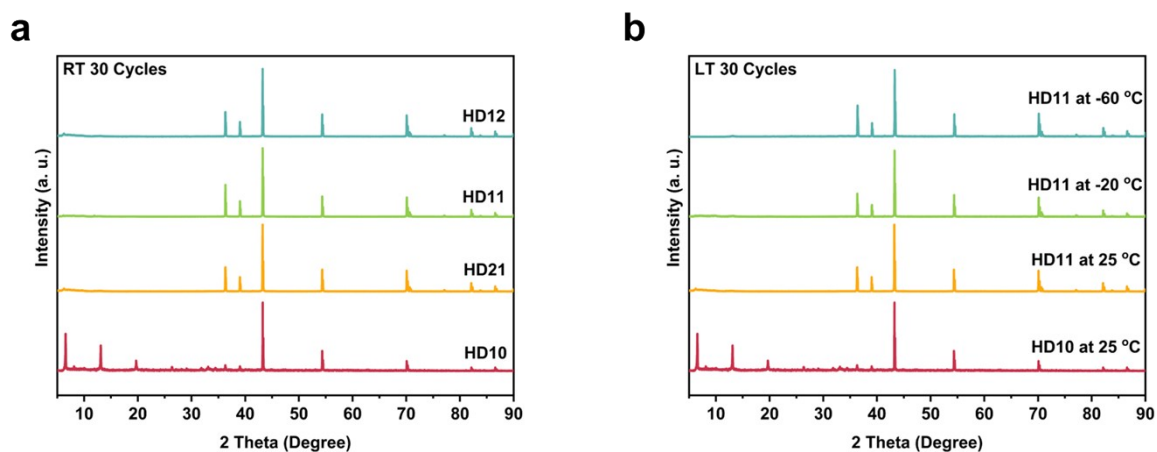
**Figure S43. XRD patterns of Zn anodes**



**Fig. S43** X-ray diffraction (XRD) characterization for crystal structure Zn anodes in Zn//Zn symmetric cells with ZFE and hybrid electrolytes after 30 cycles at room temperature (a) and different temperatures (b).

**Figure S44. Rate performances of Zn||V$_2$O$_5$ batterie with ZFE at different current densities.**
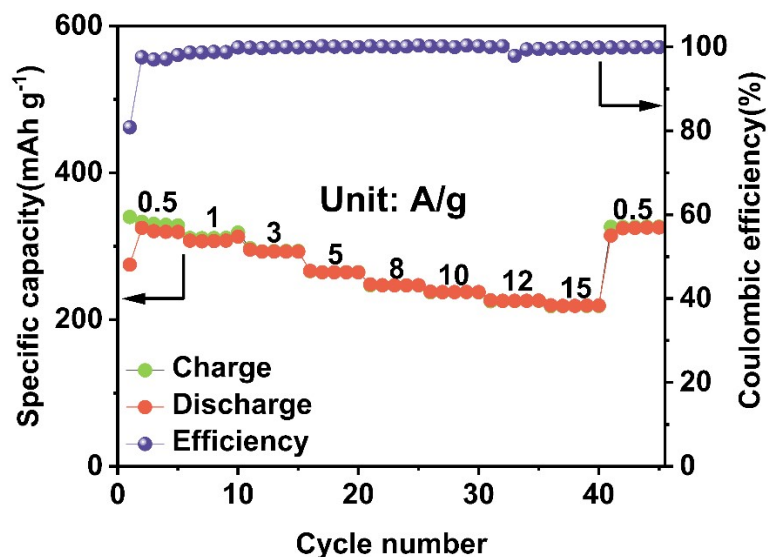


**Fig. S44** Rate performances of Zn||V$_2$O$_5$ batterie with ZFE at different current densities.

## Reference

[1]  Z. Qu, Y. Muhammad, W. He, J. Li, Z. Gao, J. Fu, S. J. Shah, H. Sun, J. Wang, Z. Huang, *Chem. Eng. J.* **2021**, 404, 126570.

[2]  a)A. Chami Khazraji, S. Robert, *J. Nanomater.* **2013**, 2013, 1; b)V. A. Basiuk, *J. Comput. Theor. Nanosci.* **2008**, 5, 2114.

[3]  S. Plimpton, *J. Comput. Phys.* **1995**, 117, 1.

[4]  A. K. Rappé, C. J. Casewit, K. Colwell, W. A. Goddard III, W. M. Skiff, *J. Am. Chem. Soc.* **1992**, 114, 10024.

[5]  H. J. Berendsen, J. R. Grigera, T. P. Straatsma, *J. Phys. Chem.* **1987**, 91, 6269.

[6]  W. Humphrey, A. Dalke, K. Schulten, *J. Mol. Graph.* **1996**, 14, 33.

[7]  O. Borodin, M. Olguin, P. Ganesh, P. R. Kent, J. L. Allen, W. A. Henderson, *Phys. Chem. Chem. Phys.* **2016**, 18, 164.

[8]  a)N. Michaud-Agrawal, E. J. Denning, T. B. Woolf, O. Beckstein, *J. Comput. Chem.* **2011**, 32, 2319; b)R. J. Gowers, M. Linke, J. Barnoud, T. J. Reddy, M. N. Melo, S. L. Seyler, J. Domanski, D. L. Dotson, S. Buchoux, I. M. Kenney, presented at *Proceedings of the 15th python in science conference*, **2016**.